Resonant Fluorescence Spectroscopy in Low Dimensional Semiconductor Structures

by

Pranshu Maan

A dissertation submitted in partial fulfillment
of the requirements for the degree of
Master's of Science
(Electrical Engineering and Computer Science)
in The University of Michigan
2017

Thesis Committee:

Associate Professor Hui Deng, Chair
Associate Professor Pei Cheng Ku, Co-Chair
Professor Duncan Steel
Professor Mackillo Kira

To my Parents: for your hard work and sacrifices and Teachers: for your guidance and support

ACKNOWLEDGEMENTS

I could not be more indebted to my advisor Prof. Hui Deng for her patience and guidance throughout my research. At the time I joined her group, I had no background in Physics, and had never worked in an optics lab. Foreseeing the challenge that lied ahead of me, Prof. Deng decided to guide me despite of my non Physics background and her busy schedule, for everything is impossible until it is done. I was fortunate that Prof. Deng allocated a dedicated lab space to me, where I started from scratch, learned basic optics lab fundamentals, tricks involved in building the setup, and performing resonant fluorescence experiment. It was here I was introduced to quantum optics and quantum information, learned to use lasers and other optical measurement techniques. Even during the program when I was doing research, taking courses as a full-time student and working full time 20 miles from the campus (and I did not know to drive that time), Prof. Deng always made sure that I am able to manage my responsibilities. It is a privilege for me to be her first MS student.

I would not have made this far without constant support from Prof. Pei-Cheng Ku. While I was trying to figure out what courses conforms to my research interest, it was only after taking the course in semiconductor optoelectronics, I was able to decide what courses I would be interested in. It was during this course work I was introduced to basics of semiconductor optical processes and GaN based LEDs. I am grateful to Prof. Ku for accepting my request to be co-advisor from Electrical department. Participation in bi-weekely team meeting was always a privilege for

me. At the time when it was not possible for me to be present for the GaN group meeting, Prof. Ku helped me out to ensure I dont miss the group meeting, and was always available for guidance. Without his support this thesis would never have been written.

I would like to thank Prof. Duncan steel and Prof. Mackillo Kira, not only for accepting my request to be on the thesis committee, but also for introducing me to quantum mechanics and quantum electrodynamics. Being a challenging coursework, I would not have managed to continue my research, full time work and course load without his support.

I will always be grateful to all the members of Deng lab for their guidance and support. I would like to thank Zhaorong for guiding me to undergo transformation from non Physics background by helping me in choosing right courses. You were right that it will not be easy but it can be done. I would like to thank Glenn for handing over to me height marker on my first day in the lab. Without this guiding tool I would have never come this far. I am grateful to Tyler for all his support. Your support was a critical component in my transition. I also like to thank you for accepting and participating in review discussion. This section will be incomplete without mentioning support from Adam. It was my privilege to work with you in initial days. It was during this time I got to learn how to critically evaluate any topics. I cannot thank you more for answering my questions irrespective of how basic it was. Thank you for always evaluating my approach and making sure I am on right track, and for giving me heads-up for the potential difficulty involved in the experiment. This thesis would have been incomplete without the support from Long. I would like to thank you for always finding some time to discuss my questions irrespective of your very busy schedule. It was during one instance when I did not

had any sample to work on, you specially fabricated a sample for me. If it wasnt you, I would have never learned basics of optics setup. I would like to thank Tim for making pair of excellent samples for my experiment, otherwise it would be difficult to observe resonance fluorescence. I would like to mention support from Jiaqi for always finding time to discuss my questions. I would like to thank Jason, Eunice and Hoon for your support. I would also like to thank Brandon, Kunook, Jingyang from Prof. Ku group for your support and inputs.

I would like to thank Aaron Ross from Prof. Steels group in introducing us to experimental technique for resonance fluorescence in quantum dots, and for helpful discussions.

I would like to thank John Prescott from the International center for helping me in immigration-related topics.

I thank Prof. RM Vasu, IISc and all my teachers for their support and hard work.

I thank my friends: Dominic from Texas, Shyam from Ohio, Jacob from Netherland and Deepak from India for all your support.

It goes without saying, I would not have ever come this far without unmatchable support from my parents and my sister.

I would like to thank everyone who has supported me in this endeavor.

Pranshu Maan

Ann Arbor

December, 2017

LIST OF FIGURES

Figure

TABLE OF CONTENTS

ABSTRACT

Resonant fluorescence spectroscopy in low dimension semiconductor structure

by

Pranshu Maan

Chair: Hui Deng

Co-Chair: P C Ku

Linear quantum computation and teleportation requires interference of two single photons pulses. These photons must be indistiguishable i.e. must have same pulse width, arrival time etc. .Moreover, "if the radiative transition between two quantum states of single emitter is broadened due to spontaneous emission, single photon pulse width is fourier transform limited" and can generate indistingushable photons[4].Resonant fluorescence does not have any jitter in photon emission due to absence of non-radiative relaxation process. "Nonclassical light can be generated by resonant excitation of individual emitters to scatter single photon with coherence property determine by laser source". This creates a prototype quantum optical circuit and provide a test bed for all optical generation, distribution, and detection of nonclassical light on a common photonic chip for semiconductor based photonic information technology[Reithmaier et al.]. Moreover, resonance fluorescence is used in high fidelity readout of trapped ion qubits, and "resonant coherent excitation on

quantum dot has proven to be very efficient for achieving on high degree of indistinguishability and coherence" [4].

CHAPTER I

Resonance fluorescence and its application in Quantum Information Science

Resonant fluorescence had been studied in the 1960s in power spectrum of two-level atomic system driven near resonance by classical electric field[1]. At present it has become one of the key techniques in the generation of indistinguishable photons for linear quantum computation, quantum teleportation experiments[4], read out of qubit in trapped ion [2] or cavity electrodynamics[3] based quantum information techniques. In this work, we study resonance fluorescence in GaN based quantum dots and MX_2 based monolayers for quantum information application. Feasibility of observing resonance fluorescence in GaN based quantum dot is theoretically analyzed. For quantum information application at room temperature, the generating device must have high probablility of on demand single photon. In conventional approach involving higher band excitation, quantum dot is excited with laser having energy higher than the transition energy. One of the disadvantages of such technique is that, in due process, multiple carriers are generated. Consequently, photon generation under such conditions becomes a probabilistic in nature. Moreover, in application like quantum teleportation experiments that requires indistinguishable photon source: having same pulse witdth, arrival time etc., conventional technique of higher band excitation will suffer with non radiative phenomenon leading to time

jitter in the generation of indistinguishable photons. In order to realize single photon source at room temperature suitable for quantum information protocol, we study resonance fluorescence in GaN quanum dots. Incase of Monolayer transition metal dicalcogenides (MX_2), where light matter interaction in atomically thin MX_2 is very strong, time resolved photoluminescence measurements had been used for estimating radiative lifetime of excitons. Unfortunately, these photoluminescence results depends on material defects and impurities, and population decay of the excited state is affected by presence of dark states[9], rendering estimation of radiative lifetime of excitons using photoluminescence measurement alone difficult. Inorder to overcome this difficulty, the monolayer sample is resonantly excited. In our study, we perform resonance excitation spectroscopy of exfoliated MX_2 based monolayer sample at room temperature.

1.1 Introduction to Quantum Information

Quantum Information involves the study of information processing using a quantum mechanical system. Advances have been achieved in the study of such systems with the advent of experimental techniques to control and manipulate the quantum system such as: application of penning trap for trapped ion quantum computation(Wineland et al. 1973), application of quantum dot for single photon generation for quantum information[5], optically driven quantum dot for quantum computation[6]. This ability to generate, control and manipulate the quantum system holds the key towards the implementation of a quantum information system.

One of the key applications of Quantum information processing is towards the realization of high precision sensors that can overcome standard quantum limit due to statistical fluctuation. Moreover, quantum entanglement overcomes shot noise

limit that can find application in realization of chemical and biological sensors such as measuring concentration of blood protein[47] etc.. Further, relativistic quantum metrology framework enables realization of high precision acceleration sensor for detecting gravitational anomalies in space[8].

Quantum computation yet another frontier of quantum information. Proposal of Deutsch's model for quantum computation initiated a discussion of the existence of an even superior form of quantum computation than Church-Turing thesis[6]. Moreover, Shor's algorithm for factorization, and Grover's search algorithm over unstructured space were some of the key driving motivations toward race for quantum computers[7].

1.2 Quantum information: Application of Resonance fluorescence

1.2.1 Quantum information using trapped ion

To implement any quantum algorithm, experimental setup system must satisfy so called DiVincenzo criteria[10]. The fifth criterion underlines that for any given qubit after processing or computation, it must be read out or measured. In case of trapped ion system[2], an ion such as Al ion is confined using Paul's trap. In this arrangement, trapping field and field to change the state of the qubit is provided by set of DC and RF electrodes. If two hyperfine level of ground state of Al ion is represented by —0¿ and —1¿ respectively, then using a laser beam in resonance with atomic transition, electron can be excited to one of the hyperfine levels. If the qubit was in —1¿, then on an application of resonant excitation, the fluorescent signal can be detected using CCD camera. In this work, we demonstrate the phenomenon of resonance fluorescence in monolayer sample of MX2 material at room temperature.

1.2.2 Quantum information using quantum dot

Quantum dot is yet another approach towards realization of scalable quantum computer architecture. Solid state quantum dots or "artificial atoms" are commonly used in the implementation of quantum information due to its discrete energy levels and flexibility to tune its properties during the process of fabrication.Here, we are insterested in understanding the realization of room temperature quantum information storage device using GaN quantum dots.

Trion is a quasiparticle that can be either negative, consisting of pair of electrons and hole, or positive, consisting of pair of holes and an electron. When trion state decays off via spontaneous emission process, the polarization state of the emitted photon is entangled with the spin state of the quantum dot. Idea is to establish a strong light coupled coherent Quantum Dots (QD) system[13] and tune these QDs to optical mode of the cavity thereby creating a node. Consequently, photon thus generated can interact with both of these QDs connected via an integrated optical waveguide. In order to read out spin information, resonance fluorescence can be used to map a particular spin state to excited state population. This can further decay off emitting photons that can be detected by an appropriate photodetector.

In this work, we study the feasibility of observing resonance fluorescence in GaN based quantum dot structures.

1.3 Chapter summary

In this chapter resonance fluorescence is introduced from quantum information perspective. Primary conation of this study is to analyze the feasibility of observing resonance fluorescence in GaN based quantum dots, and realize the same in MX_2 based monolayer sample.

CHAPTER II

Introduction to III-Nitride based semiconductor quantum dots

Solid state quantum dots are zero dimensional semiconductor nanostructures, also known as "artificial atoms", providing 3D confinement to carriers. The 3D confinement results in discretization of energy states of confined carriers, leading to electron and hole localization. This discretization of energy levels of the carriers and localization of the carriers resembles an atom.

Solid state quantum dots find application as non classical light source for on demand generation of single photon[14,15] in quantum communication[16], precision measurement[17,18] and random number generation[19]. Additionally, quantum dots are commonly used for the generation of entangled photon source by using indistinguishable photon source[20,21] or from biexciton to exciton transition[22,23]. These semiconductor nanostructures can be grown either by self-assembled process or site controlled process. Those quantum dots which are self assembled, exhibit random spectral and spatial properties as a result of which they cannot be scaled and integrated with photonic components. Also, self assembled quantum dots require low temperature for operation to maintain three dimensional confinement[12]. In order to overcome these issues, III-N based site controlled quantum dots are developed. Site controlled wide band quantum dots overcome the issue of scalability and require-

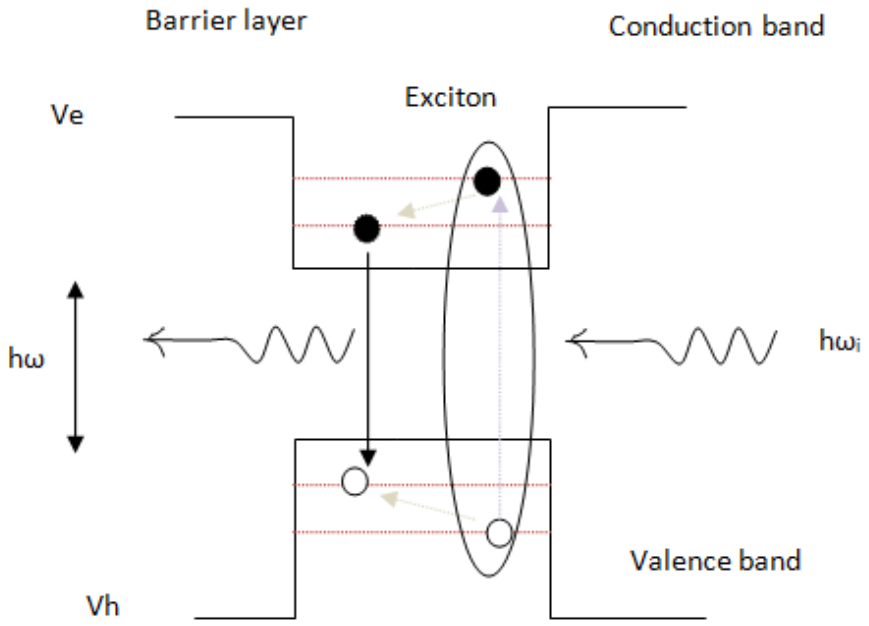

Figure 2.1: Light matter interaction in quantum dot.

ment for higher operating temperature. InGaN/GaN based quantum dots have been thoroughly investigated by [12] and optically pumped single photon source upto 90K and electrically driven single photon source upto 10K have been demonstrated. In this theses, all estimations are based on the quantum dot developed in [12].

2.1 Light matter interaction in Quantum Dots

Quantum Dots interact with photons through formation of excitons or recombination. Figure 2.1 represents interaction of quantum dot with photon and formation of exciton. We can express wavefunction of the exciton in terms of wannier function as electrons and holes are localized in near vicinity of its center of mass[24]. If m_e and m_h represents effective mass of electron and hole respectively, then Hamiltonian

for exciton can be expressed as:

$$H = -\frac{\hbar^2}{2m_e}\nabla^2_{R_e} - \frac{\hbar^2}{2m_e}\nabla^2_{R_h} - \frac{e^2}{\epsilon|r_e - r_h|} + V_\delta \tag{2.1}$$

where V_δ is perturbation term due to confinement potential for electron and hole as shown in figure the 2.1 and R_e, R_h are postion of unit cell. Further, the exciton wave function can be written as:

$$\psi(r_e, r_h) = \sum_{R_e R_h} \phi(R_e, R_h) W_{R_e}(r_e) W_{R_h}(r_h) \tag{2.2}$$

$\phi(R_e, R_h)$ is exciton envelop wavefunction and wannier funcition for electron and hole can be written in terms of Bloch state as:

$$W_{R_e}(r) = \frac{1}{\sqrt{N}} \sum_k e^{-ik\cdot R_e} \psi_k(r) \tag{2.3}$$

$$W_{R_h}(r) = \frac{1}{\sqrt{N}} \sum_k e^{-ik\cdot R_h} \psi_k(r) \tag{2.4}$$

Here, N is number of primitive cell in crystal. From the equation 2.1, we can write the Schrodinger equation in terms of center of mass of exciton as:

$$\frac{-\hbar^2}{2M}\nabla_R^2\psi(R) = E_R\psi(R) \tag{2.5}$$

where R is coordinate of center of mass and M is the total mass of exciton.

We can further treat exciton alone as free particle and we can write equation for wavefunction for center of mass. We can further describe wave function for free exciton considering their center of mass using generic solution to time dependent Schrodinger equation:

$$\psi(R,t) = \frac{1}{\sqrt{2\pi}}\int_{-\infty}^{+\infty}\phi(K)e^{i(KR-\frac{\hbar K^2}{2M}t)}dK \tag{2.6}$$

Initial wave function can be written as;

$$\psi(R,0) = \frac{1}{\sqrt{2\pi}}\int_{-\infty}^{+\infty}\phi(K)e^{iKR}dK \tag{2.7}$$

The solution to the equation above can be obtained using Fourier transform:

$$\phi(K) = \frac{1}{\sqrt{2\pi}}\int_{-\infty}^{+\infty}\psi(R,0)e^{-iKR}dR \tag{2.8}$$

and the eigen value can be expressed as:

$$E_R = \frac{\hbar^2K^2}{2M} \tag{2.9}$$

$K = k_e + k_h$

As shown in figure 2.1, one of the methods for creation of exciton is by photon absorption. Interband absorption of photon with energy $\hbar\omega_i$ can occur anywhere in the Brillouin zone where:

$$\hbar\omega_i = E_c(K) - E_v(K) \tag{2.10}$$

corresponding to conduction and valence band respectively.

and

$$\nabla_K E_c(K) = \nabla_K E_v(K) \tag{2.11}$$

The equation above describes the fact that for absorption and hence for the formation of exciton, group velocities of electron and hole must be equal allowing for coulombic interaction[24].

We can further write decoupled equation of relative motion for electron and hole as the coulomb interction is independent of center of mass coordinate.

$$\frac{-\hbar^2}{2\mu}{\nabla_r}^2 + V(r)\psi(r) = E_r\psi(r) \tag{2.12}$$

The equation above can be interpreted as Schrodinger equation for a particle with mass μ in a central coulombic potential.This can be treated as a simple hydrogen atom problem. By using this approach we can describe quantization of energy in quantum dots that is why it is referred to as "artificial atom". The solution to the equation can be expressed in a form containing an angular part defined by spherical harmonic term$Y_l m(\theta, \phi)$ and a radial part. Also, the equation is spherically symmetric, we can write the Schrodinger equation in spherical coordinates as:

$$[\frac{-\hbar^2}{2M}\frac{1}{r}\frac{\partial^2}{\partial r^2} + \frac{1}{2Mr^2}L^2 + V(r)]\psi(r) = E\psi(r) \tag{2.13}$$

Where first term corresponds to radial kinetic energy and second term represents rotational kinetic energy and $\psi(r)$ can be expressed as product of radial wavefunction and spherical harmonics. Further, we can express L^2 in spherical harmonics as:

$$L^2 Y_l m(\theta,\phi) = l(l+1)\hbar^2 Y_{lm}(\theta,\phi) \tag{2.14}$$

On multiplying by factor $2\mathrm{M}r_2$ and dividing with $R_{nl}(\mathrm{r})Y_{lm}(\theta,\phi)$, we can write eqn. 2.5 as:

$$[\frac{-\hbar^2 r}{R_{nl}}\frac{\partial^2}{\partial r^2}(rR_{nl} + 2Mr^2(V(r)-E)] + [\frac{L^2 Y_{lm}(\theta,\phi)}{Y_{lm}(\theta,\phi)}] = 0 \tag{2.15}$$

We can substitute $\mathrm{U(r)}=\mathrm{r}R_{nl}$ on further simplifying the equation above, we can write the equation in terms of reduced mass as:

$$-\frac{\hbar^2}{2\mu}\frac{d^2U(r)}{dr^2} + [\frac{l(l+1)\hbar^2}{2\mu r^2} - \frac{e^2}{r}]U(r) = EU(r) \tag{2.16}$$

at r=0, U(r)=0 and second term diverges and can be disregarded.

Under this boundary condition, solution to the equation above

U(r) is of the form r^{l+1} further we can subject the equation to boundary condition where r is very large. On combinig the solutions in the above mentioned boundary conditions, we can express U(r) as:

$$U(r) = r^{l+1}Q(r)e^{-\gamma r} \qquad \gamma = \sqrt{2\mu(-E)}/\hbar \tag{2.17}$$

we can assume power solution for the equation 2.8 with U(r) defined in 2.9. Solution is of the form:

$$Q(r) = \sum_{i=0}^{N} a_i r^i \tag{2.18}$$

For a valid solution equation 2.10 must terminate at some value of N i.e. corresponding coefficient must be zero. With this boundary condition, on substituting equation 2.10 in 2.8, we will find discretized energy in the form:

$$E_n = \frac{-Const}{n^2} \tag{2.19}$$

2.2 Properties of GaN

A significant portion of the research is oriented towards estimation of resonance fluorescence in GaN based quantum dots. It would be interesting to look into properties of GaN. One of the interesting properties of GaN in optoelectronic application is the presence of direct band gap in visible spectrum. However, GaN based devices suffers from dislocation due to lattice mismatch of substrate thereby affecting its optical and electrical performance[25]. For example, all the estimation in this thesis is based on GaN based quantum dot grown on c-plane sapphire substrate. Con-sequently, we can expect deterioration in optical characteristics of the device due to lattice mismatch. If the lattice mismatch with the substrate layer is small, then "stress can be relieved by nearby layer undulation"[26]. If the strain is large, depending on nature of strain, "the unit cell along the growth direction will expand or contract". Further, threading dislocation which is common in GaN is observed when dislocation from substrate propagate to layers below[26]. Figure 2.2 represents band structure of Wurtzite GaN. Direct band gap is found to be 3.5eV, whereas HH to LH gap is 6meV and split off hole and LH has gap of 37meV.

In presence of perturbation term and spin orbit coupling, Hamiltonian for GaN

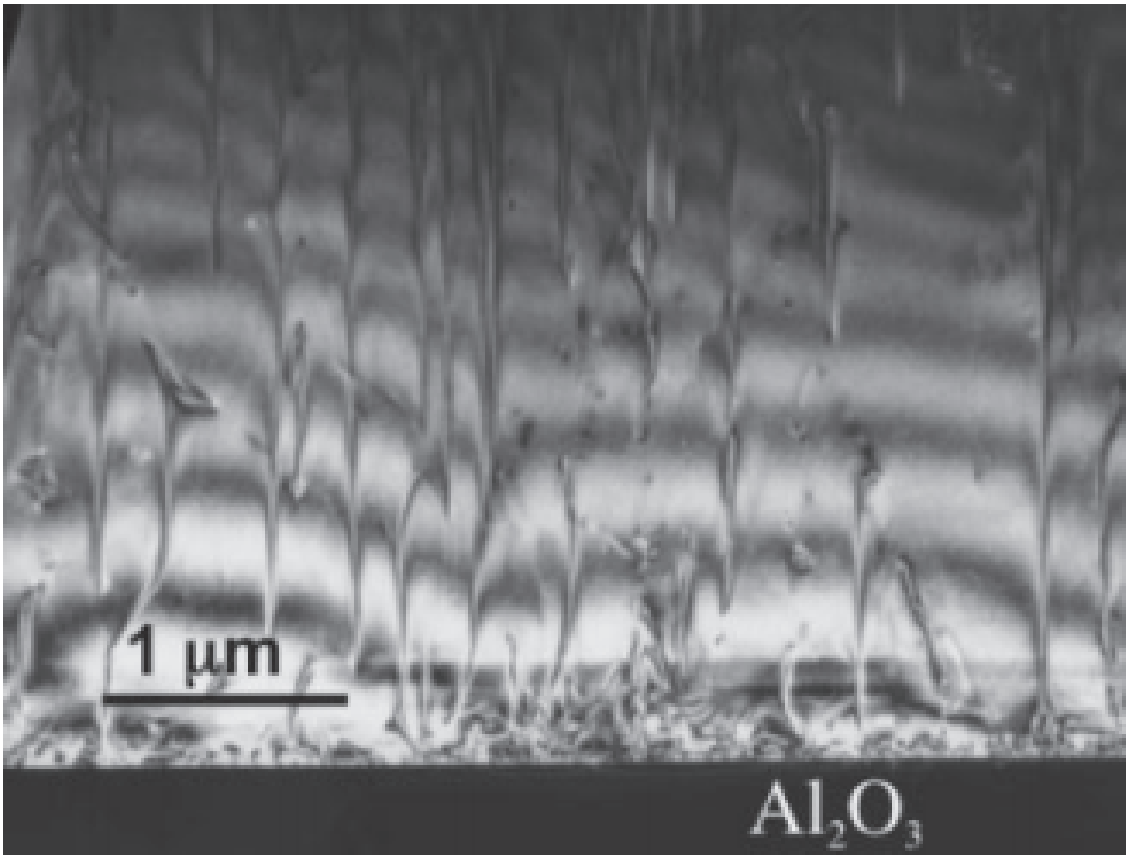

Figure 2.2: TEM micrograph image of GaN cross section grown on c-sapphire substrate[26].

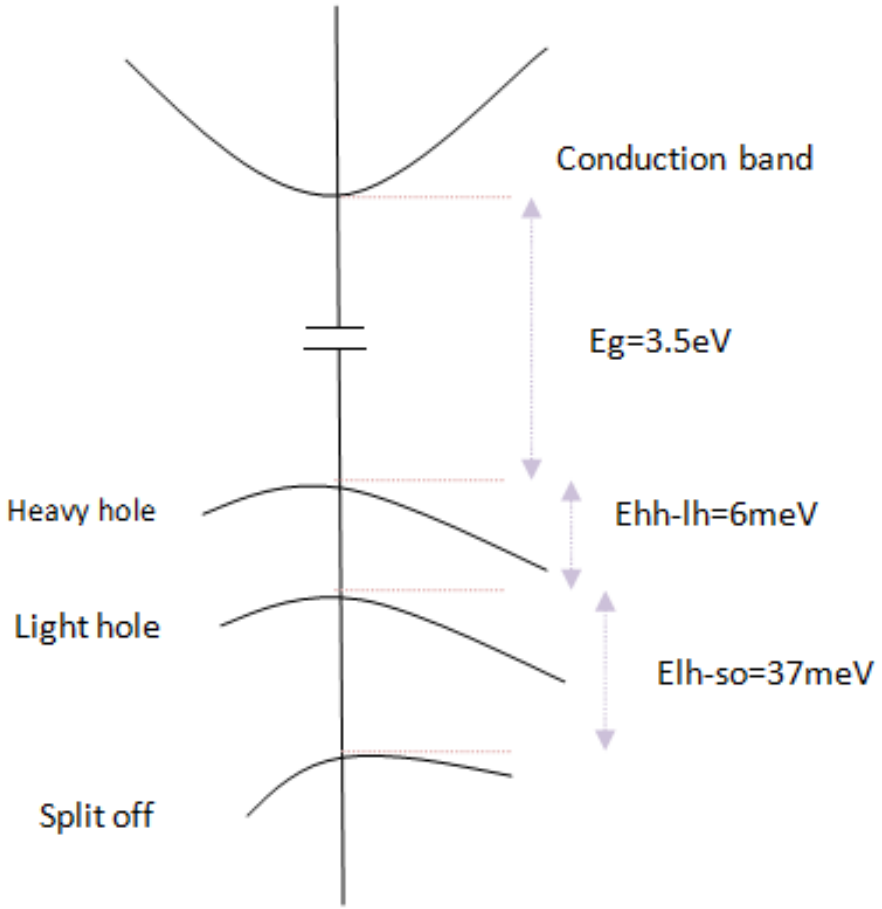

Figure 2.3: Band structure of Wurtzite GaN.

can be written as:

$$H = \frac{p^2}{2m_0} + \frac{\hbar^2 k^2}{2m_0} + \frac{\hbar}{m_0}k^2 + \frac{\hbar}{m_0}k * p + V(r) + \frac{\hbar}{4{m_0}^2 c^2}\nabla V p * \sigma \tag{2.20}$$

here scalar product k*p is the perturbative term expressed as:

$$k * p = k_x(-i\hbar\frac{\partial}{\partial x}) + k_y(-i\hbar\frac{\partial}{\partial y}) + k_z(-i\hbar\frac{\partial}{\partial z}) \tag{2.21}$$

last term in the equation 2.21 represents contribution due to spin orbit coupling.

2.3 GaN based semiconductor quantum dot

In this thesis, estimation of resonance fluorescence signal from GaN based quantum dot is based on the quantum dot developed by[12]. It would be useful to understand the properties of the quantum dot. The structure consists of disk in nanowire which is basically a truncated cone shaped GaN pillar. Each disk is made of a 3nm thick $In_{0.15}Ga_{0.85}N$ nano disk in a 120nm tall GaN pillar.Nano disk is further characterized by 10nm thick GaN at the top, and has sidewall slope of 75°. Structure of nanopillar has great influnce on the emission signal from the quantum dot. "First lens collection efficiency is defined the ratio of far field within collection cone of ob-jective lens and total radiation power". The collection efficiency from these dots are affected by diameter of the nano disks, radial position of the dipole and polarization of the dipole[12]. It has been observed that the first lens collection efficiency de-creases with increase in the diameter of the nanodisk. This is because portion of the emitted signal is internally reflected from GaN air interface. [12] has underlined that although ND with smaller diameter can have better first lens collection efficiency, it has detrimental effect on the local density of photon state which directly depends on the size of the nanodisk. To optimize the design, it has been suggested that con-formal coating the sample with GaN layer enhancement in local density of photon

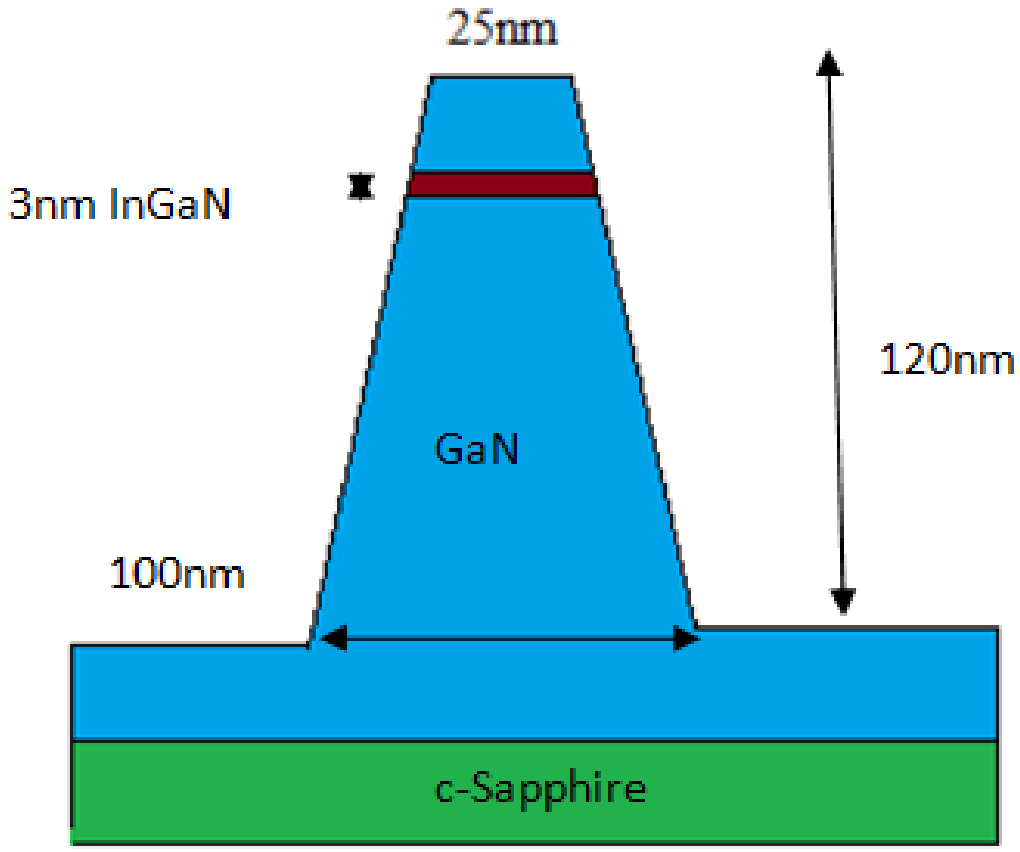

Figure 2.4: Representation of single GaN nanopillar with InGaN nanodisk.

state can be achieved without affecting the first lens collection efficiency, and first lens collection efficiency of 15% can be maintained. Moreover, it has been reported that first lens collection efficiency averaged over entire nanodisks for all polarization varies from 2% for quantum well limit to 30% to quanutm dot limit.

Another factor that affects the first lens collection efficiency is position of dipole emitter[27]. It has been observed that in case of small nanopillars emission in free space mode is relatively better than large nanowires. In large nanowires emission is coupled into two guided HE_{11} modes[28]. The one propagting in upward direction is reflected back from the GaN air interface into the substrate.

2.4 Summary

Light matter interaction in quantum dots is discussed. Further, discretization of energy in quantum dots has been explained in detail. In the subsequent section, material property of GaN and defects in GaN has been discussed. Further, band diagram for GaN has been introduced. In the last section, quantum dot used in this thesis for theoretical estimation of resonant fluorescence signal has been explained.

CHAPTER III

Optical properties of TMDC materials

3.1 Structure of TMDCs

Transition Metal DiChalcogenides (TMDC) are atomically thin 2D materials. They consist of transition metals like Tungsten sandwiched between DiChalcogenides layers like Se. In bulk TMDCs are indirect bandgap material, and monolayer sample of TMDCs are direct bandgap material with hexagonal crystal structure as shown in figure 3.1. This transition from indirect band gap to direct band gap is due to inter layer hopping. Direct band gap can be found at the extrema of band edge in the hexagonal crystal lattice, also known as +/-K points.

In case of monolayer sample valence band maxima and conduction band minima are located on the corners of the first Brillouin zone of the hexagonal crystal lattice at the K points. At the band edge of valence band at K points, d_{xy} and $d_{x^2-y^2}$ of transition metals hybridize with p_x and p_y orbitals of chalcogen atoms. On the band edge of conduction band minima, $d_{3z^2-r^2}$ from transition metal hybridizes with p_x and p_y orbitals of chalcogen atoms. These orbitals are localized in xy plane[29].

One of the important properties of TMDC monolayer is strong light matter interaction. It can absorb around 10 to 20% of incident light. Optical conductivity of

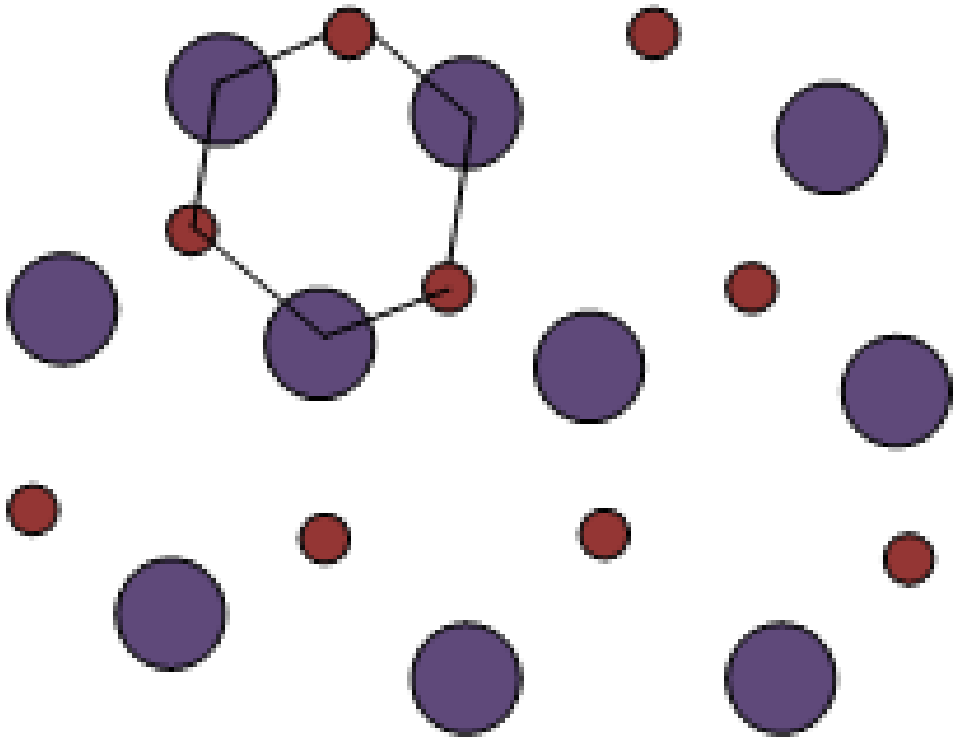

Figure 3.1: Crystal lattice structure of TMDC, top down view.Red dot represents chalcogen atoms, blue dot represents Transition metal atoms.

material is given by[29]:

$$\sigma(\omega) = A(\omega) \sum_{v,c} \frac{1}{2\pi^2} \int_{S_\omega} \frac{dS}{|\nabla_k (E_c - E_v)|} |d_{vc}|^2 \tag{3.1}$$

In the equation 3.1, $\sigma(\omega)$ diverges if $|\nabla_k (E_c - E_v)| = 0$. This can be intepretated as peak in optical conductivity and term within the integral sign as joint density of states. The divergence condition with $|\nabla_v| = |\nabla_c|$ occurs where conduction band is parallel to valence band. This is also known as band nesting[29]. Minima of conduction and maxima of valence band is located at K/K- at each corner of the hexagonal lattice in the first brillouin zone. These K points exhibit time reversal symmetry and unlike in graphene, it exhibits broken inversion symmetry[29,33]. So, theoretical modeling of TMDCs involves starting with graphene and introducing staggered sub-lattice potential to break inversion symmetry[33]. This affects the spin orbit coupling term in the Hamiltonian. Consequently, spin splitting is dependent on the variation of band maxima/ minima, or valley. Also, "due to this lack of inversion symmetry, bands are split by intrinsic spin orbit coupling except at points where time rever-sal symmetry is preserved" i.e. Valence band located at K points will exhibit spin splitting and spin polarization[33].

In figure 3.2, spin split in conduction and valence band is denoted by $2\Delta_{cb}$ and $2\Delta_{vb}$ These valleys exhibit non equilibrium charge imbalance, and absorbs left handed polarized differently than right handed polarized light[32]. This K dependent degree of polarization between maxima of valence band and minima of conduction and is given by:

$$\nu(k, \omega_{cv}) = \frac{|P_+{}^{cv}(k)|^2 - |P_-{}^{cv}(k)|^2}{|P_+{}^{cv}(k)|^2 + |P_-{}^{cv}(k)|^2} \tag{3.2}$$

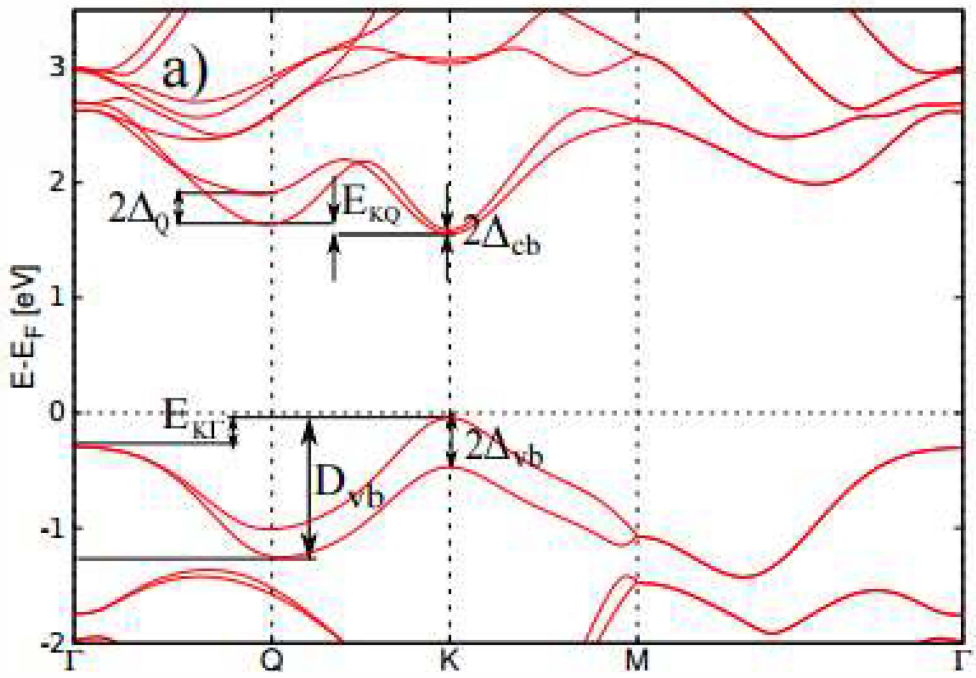

Figure 3.2: Band diagram of TMDC[33]

The equation above represents normalized difference in degree of absorption be-tween right hand and left hand polarization between valence and conduction band[32].

3.2 Luminescence properties of TMDC

Indirect band gap to direct band gap transition has a significant impact of luminescence properties of TMDCs. This transition from multi-layer to monolayer can be observed from the shift in PL peak towards higher energy and increase in PL intensiy counts.This decrease can be gradual as observed in chemically exfoliated MoS_2, but there was a sharp drop in quantum yield from a monolayer to bilayer in case of mechanically exfoliated MoS_2. This gradual decrease has been explained as a consequence of weaker interlayer coupling due to rotational stacking disorder[29,30].

PL emission intensity also depends on the ambient temperature. In case of single layer MoS_2, PL intensity was observed to decrease with temperature, but for few

layers it increases with temperature. The decrease in PL intensity is usually due to increase in non radiative recombination process. However, unsual behavior in few layers is due to degenerate direct and indirect band gaps.Further simulation[31] confirmed the behavior attributed to thermal decoupling of nearby layers by thermal expansion.

Interestingly for ReS_2, PL intensity decreases from monolayer to bulk[Tongay et al. 2014]. The band gap simulation for ReS_2 shows that bandgap is direct for both monolayer and bulk due to weak interlayer coupling. Consequently, bulk of ReS_2 behaves as 2D material.

Source of single photon has been found in WSe_2 monolayer samples. It was noted when certain region of the sample was excited, it resulted in emission characterized by high intensity and narrow linewidth[Koperski et al. 2015]. These narrow linewidth emission also exhibited photon antibunching confirming the emission of single photon source and three dimensional confinement.

Origin of single emitters are not yet clear. It has been found that these single emitters occurs along the edge of WSe_2 monolayer and at the interface of monolayer and multilayer. Irrespective of location, these single emitters are understood to originate from crystal defects. These single emissions obtained from the edges of monolayer sample were robust against ambient conditions withstanding temperature cycles. However, the emission characteristic if noisy and exhibit time scale jitter in the order of linewidth, can be improved by resonantly exciting the sample.

Photoluminescence tuning is another important concept towards the realization of resonance fluorescence in charged excitons. Photoluminescence tuning in TMDCs has been studied by the application of hydrostatic pressure, uniaxial strain, and electrical

gating of the sample in field effect transistor arrangement[29]. Enhancement in PL intensity was observed for MoS_2 monolayer sample when the applied gate voltage was varied from -50V to +50V, while zero phonon line wavelength was nearly constant. No enhancement in PL was observed for bilayer MoS_2. For WS_2 samples PL for monolayer was observed to reduce on application of gating voltage, while in case of bilayer WS_2 it increases on application of lateral electric field[Newaz et al. 2016].

For resonance fluorescence excitation, it would be interesting to observe change in emission pattern by tuning the bandgap. In the current setup, excitation wavelength was scanned through the entire wavelength range in steps of 1nm. Since the suppression is very sensitive to wavelength, for each excitation wavelength, the setup was optimized to suppress the background laser. By employing the band tuning technique, we can optimize the setup to suppress background laser and simply tune the bandgap by applying the gate voltage.

3.3 Excitons in TMDCs

In chapter 2 we have discussed the formation of excitons. In ionic crystals where dielectric constant is large, the binding energy of E-H pair is high (upto eV). These excitons are called Frenkel excitons. Whereas in semiconductor materials, the dielctric constant is relatively large. Additionally, due to electric field screening, coulombic interaction is reduced. So, exciton radius is larger. These excitons are called Wannier excitons as we can include the effect of lattice potential in the exciton wavefunction. Exciton binding energy is expressed as[29]:

$$E_n = -\frac{E_0}{(n + \frac{\alpha-3}{2}^2)} \tag{3.3}$$

where α is dimensionality of the system, n is principal quantum number and E_0

is the exciton rydberg. For monolayer sample, impact of dielectric screening is less as excitons are confined in 2D plane. So, we observe stronger binding energy than in bulk. As a consequence, excitons are large enough and have high binding energy i.e they can be modelled as Wannier type and Frenkel type excitons.

For 2D materials, it has been shown that only circularly polarized lights couple to bandedge located at K points[35] as a consequence of inversion asymmetry. Consequently, exciton in single valley can emit circularly polarized light. In order to obtain linearly polarized emission exciton emission must be in coherent superposition from two valley states[35]. Although, emission from neutral exciton is circularly polarized, when the monolayer is excited with linearly polarized light, resulting emission from neutral exciton is highly polarized and emission of H component photoluminescence is stronger than V component. So, right handed light couples to -K and left handed light couples to +K valleys. When we excite a sample using linealy polarized source, it can be considered as coherent superposition of left and right handed circular polarization. So, it will excite both +K and -K, thereby converting quantum coherence to valley coherence[36].

$$\sum_{q} a(q)(e^{-i\theta}\hat{e}^{+}_{-K+\frac{q}{2},\downarrow}\hat{h}^{+}_{+K-\frac{-q}{2},\uparrow} + e^{+i\theta}\hat{e}^{+}_{K+\frac{q}{2},\uparrow}\hat{h}^{+}_{-K-\frac{-q}{2},\downarrow})|\phi> \tag{3.4}$$

In the equation above, "a(q) is coefficient of linear combination and q is wave vector measured from point K. $|\phi>$ represents intial band condition where conduction band is completely free and valence band is occupied. $\hat{e}^{+}_{K+\frac{q}{2},\downarrow}$ creates spin down electron in conduction band with momentum K and correspondingly, $\hat{h}^{+}_{-K+\frac{q}{2},\uparrow}$ creates spin up hole with momentum -K in valence band". Since emission from neutral exciton is linearly polarized irrespective of the orientation of linearly polarized excitation, it represents conservation of valley coherence[36].

3.4 Summary

In this chapter band structure of TMDC was introduced. Exciton formation and luminescence properties in TMDC material were explained further to understand underlying principle and characteristics of PL emission from $WSe2$ monolayer sample.

CHAPTER IV

Resonance fluorescence in semiconductor nanostructures

Resonance fluorescence phenomenon has been studied in two level system as an interaction with driving laser whose frequency is at resonance with transition frequency of the two level system. In this chapter we will study resonance fluorescence as scattering phenomenon. We will further look into resonance fluorescence in quantum dot system and quantum well system.

4.1 Resonance fluorescence as scattering phenomenon

Consider a simple two level system with tansition frequency ω_f. When this two level system is excited with near resonance, single mode, coherent field with frequencyω_{nr}, we can expect two components in the scattered radiation: As per energy conservation we expect elastically scattered photons having frequency $\omega_{scattering} = \omega_{nr}$, also known as Rayleigh component. Associated with this scattering, we have fluorescence from atom itself. This emission has central frequency in spectrum same as the two level transition frequency.

As evident from the figure 4.1, the elastic component has its wavelength near to fluorescence from the atom. Consequently, these two components cannot be spectrally filtered. In order to observe this fluorescence from the two-level system, we must suppress the elastic component due to excitation laser.

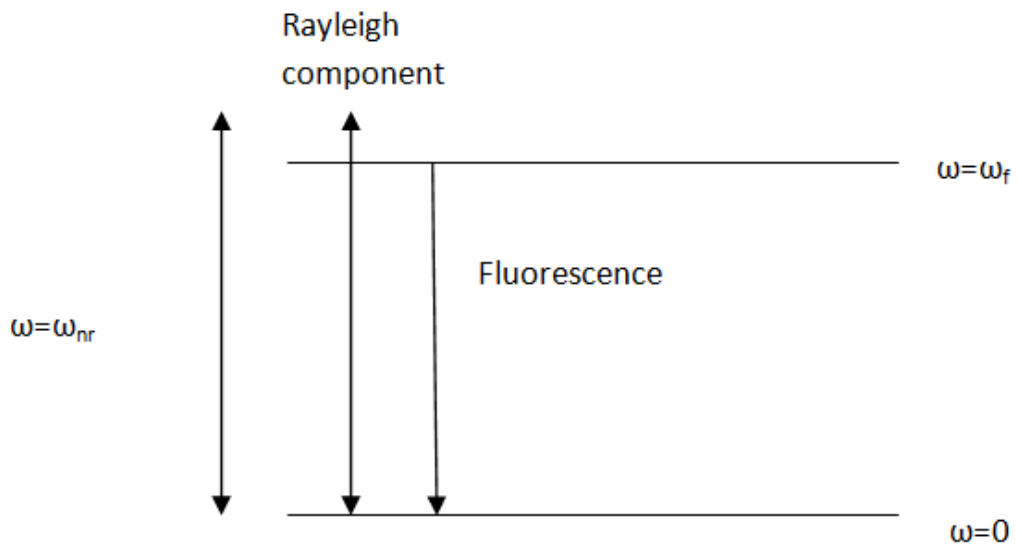

Figure 4.1: Resonance fluorescence in two level system

In two-level modeling for a single atom, assuming rabi frequency is much smaller than radiative decay rate, scattering of single mode coherent light by two level system can be spectrally written as[37]:

$$F(\omega_s) = \frac{\gamma' - \gamma}{\gamma'} \frac{\gamma'/\pi}{(\omega_0 - \omega_s)^2 + \gamma'^2} + \frac{\gamma}{\gamma'}\delta(\omega_s - \omega) \tag{4.1}$$

Equation 4.1 is significant as it explains characteristics of the resonant fluorescence emission. The first part of the equation has lineshape similar to absorption or photoluminescence of the atom. Followed by rayleigh elastic part with delta function characteristics. In the later section where we discuss resonant fluorescence spectrum for a three level quantum well system, the delta function appearing in the equation is due to rayleigh scattering.

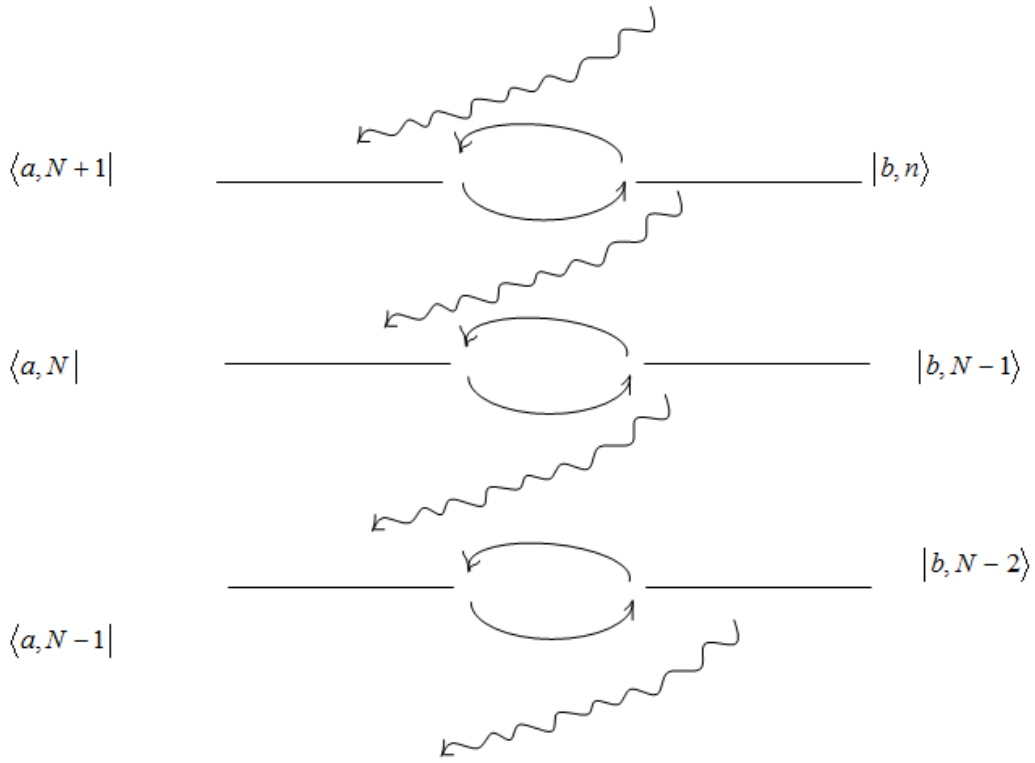

Figure 4.2: Resonance fluorescence as radiative cascade process

4.2 Resonance fluorescence as dressed atom phenomenon

Apart from semi classical Bloch equation based approach, phenomenon of resonance fluorescence can also be explained based on dressed atom approach[38]. Dressed atom exhaustively explains formation of mollow triplet, which using semi classical approach, we observe it in high rabi frequency regime. Here, we will restrict our scope to explaining the phenomenon of resonance fluorescence from dressed atom point of view.

Figure 4.2[38])represents three manifolds E(N), E(N-1) and E(N-2) consisting uncoupled state of atom laser system. The small arrow pointing towards right represents the phenomenon of absorption, and that pointing towards right represents stimulated emission. Wiggle line represents spontaneous emission process between manifolds.

As seen from the figure 4.2, while making rabi oscillation beween $< a, N+1|$and $|b, N>$, it can make quantum jump from $|b, N>$ to $|a, n>$ by the process of spontaneous emission. Before rabi oscillation between $|a, N>$ and $|b, N-1>$ can again start to undergo spontaneous emission. It would be interesting to understand the time interval between two spotaneous phenomenon. Considering first emission occurs from $|b, N>$ to $a, N>$ at t=0, next spontaneous emission will occur from $|b, N-1>$ with some delay $d\tau$, where τ is interval between two successive spontaneous emission. Distribution of τ for resonance condition is then expressed as[38]:

$$K(\tau) = \Gamma \frac{\Omega^2}{\lambda^2} sin^2(\frac{\lambda\tau}{2}) e^{\frac{-\Gamma\tau}{2}} \tag{4.2}$$

where

$$\lambda^2 = \Omega^2{}_1 - \frac{\Gamma^2}{4} \tag{4.3}$$

4.3 Resonance fluorescence in GaN based quantum dot

In this section we will look into details of resonance fluorescence from quantum dots. Based on this, we will then estimate emission profile from GaN based quantum dots. Aim of this estimation was to find out, considering characteristics of GaN based quantum dots, is it feasile to observe resonance fuorescence. We further compare the estimation for GaAs based quantum dots.

Resonance fluorescence as semi classical approach has been studied[39].

If $\hat{H}_0(r)$ is non interacting Hamiltonian of an isolated quantum system, and $\hat{V}(r,t)$ represents ineraction of time dependent, classical optical field interacting with the quantum system, we can represent the Hamiltonian as: $\hat{H}(r,t) = \hat{H}_0(r) + \hat{V}(r,t)$. If $\psi_n(r)$ represents eigenstate of $\hat{H}_0$, then we can write an arbitary wavefunction as:

$$\psi(r,t) = \sum_n a_n(t)\psi_n(r) \tag{4.4}$$

So, from Schrodinger wave equation:

$$i\hbar\frac{\partial\psi}{\partial t} = [\hat{H}_0(r) + \hat{V}(r,t)]\psi(r,t) \tag{4.5}$$

from equation 4. and 4.5:

$$\mathrm{i}\hbar\sum_n \dot{a_n}(t)\psi_n(r) = \hat{H}_0(r)\sum_n a_n(t)\psi_n(r) + \hat{V}(r,t)\sum_n a_n(t)\psi_n(r) \tag{4.6}$$

standard solution to Schrodinger wave equation can be written as:

$$H_0\left|n\right\rangle = E_n\left|n\right\rangle \tag{4.7}$$

with: $\left|\psi(r,t)\right\rangle = \sum_n a_n(t)\psi_n(r)$, we can write:

$$\mathrm{i}\hbar\sum_n \dot{a_n}(t)\left|n\right\rangle = H_0(r)\sum_n a_n(t)\left|n\right\rangle + V(t)\sum_n a_n(t)\left|n\right\rangle$$

multiplying with complex conjugate of the wavefunction and integrating it both side in equation 4.6, we can write:

$$\mathrm{i}\hbar\sum_n \dot{a_n}(t) = E_n a_n(t)\psi_n(r) + \sum_m V_{nm}(t)a_m(t) \tag{4.8}$$

In matrix notation, we can write equation 4.8 as:

$$i\hbar \dot{a_n}(t) = Ea(t) + V(t)a(t) \tag{4.9}$$

On writing elements of the matrix element V(t) and applying rotating wave approximation, we can write equation 4.9 as;

$$i\hbar \dot{a}(t) = \frac{\hbar}{2} \begin{pmatrix} -\omega_0 & {\Omega_0}^*(t)e^{i\omega t} \\ \Omega_0(t)e^{-i\omega t} & \omega_0 \end{pmatrix} \tag{4.10}$$

So, Hamiltonian can be written as:

$$H(t) = \begin{pmatrix} -\omega_0 & {\Omega_0}^*(t)e^{i\omega t} \\ \Omega_0(t)e^{-i\omega t} & \omega_0 \end{pmatrix} \tag{4.11}$$

In the equation above, if E_0 is the amplitude of the driving field, μ is the dipole moment, then we can define $\Omega_0 = \frac{\mu E_0}{\hbar}$ is called Rabi frequency.

Further, in interaction representation, we can write equation of motion as:

$$\dot{\rho_{11}}(Z,t) = -i\chi^* {\rho_{21}}'(Z,t) + i\chi^* {\rho_{12}}'(Z,t) + \gamma_2 \rho_{22}(Z,t) \tag{4.12}$$

$$\dot{\rho_{22}}(Z,t) = i\chi^* {\rho_{21}}'(Z,t) - i\chi^* {\rho_{12}}'(Z,t) - \gamma_2 \rho_{22}(Z,t) \tag{4.13}$$

$$\dot{\rho_{12}}(Z,t) = -(\gamma - i\delta_) {\rho_{12}}'(Z,t) - i\chi^*(Z,t)[\rho_{22}(Z,t) - \rho_{11}(Z,t)] \tag{4.14}$$

$$\dot{\rho_{21}}(Z,t) = -(\gamma + i\delta_) {\rho_{21}}'(Z,t) + i\chi^*(Z,t)[\rho_{22}(Z,t) - \rho_{11}(Z,t)] \tag{4.15}$$

and $\chi(Z,t) = -\mu \frac{E_0(Z,t)}{2\hbar}$

Here we are interested in finding excited state population ρ_{22}.

In steady state condition,

$\dot{\rho_{22}}(Z,t) = 0$

i.e.

$$\rho_{22} = \frac{\frac{2\gamma}{\gamma_2}|\chi(Z)|^2}{\gamma^2 + \delta^2 + 4\frac{\gamma}{\gamma_2}|\chi(Z)|^2} \tag{4.16}$$

Intensity of emitted fluorescence can be expressed as:

$$Intensity = \rho_{22}\gamma_2\eta\tau \tag{4.17}$$

where γ_2 is excited state decay rate, η is setup detection efficiency, τ is integration time. Based on this theory, we report feasibility of observing resonance fluorescence in GaN based quantum dots. Further, we compare the estimation with GaAs based quantum dots.

Based on the setup in the figure: considering objective lens collection efficiency with solid immersion lens on the sample as 70% (typical value from literature comparison). We consider 50% of transmission due to beam splitter, in 400nm, detector efficiency for picoquant SPAD 9%, 50% transmission loss through cross polarizer, coupling efficiency into single mode fiber of 50%. Also, by choosing solid immersion lens we can reduce beam spot size forming on the sample, thereby increasing the intensity for given excitation power. We are using GT polariser which has exctinction ratio of 10^5. Also, considering signal efficiency due to absorption in sample to be 70% at given wavelength range of 400nm, we expect beam spot size of 259.5nm.

Also,

$$Intensity = \frac{Power}{\pi\frac{beamspotsize^2}{4}} \tag{4.18}$$

Once we obtain intensity for given input power, we can find electric field as: $Electricfield = \sqrt{\frac{Intensity}{\eta_{GaN} c \epsilon_0}}$

c and ϵ being constant. Here η_{GaN} is refractive index= 2.53 for GaN. This excited state decay time is related to dipole moment as:

$$\gamma_2 = \frac{\omega^3 \eta |\mu|^2}{3\pi\epsilon_0 \hbar c^3} \tag{4.19}$$

with η is refractive index = 2.53 for GaN and μ is the dipole moment in terms of Debye. 1D approximately = 3.34x10^{-34} C m. From the equation above, we find dipole moment for GaN to be around 8D.

With 1meV=1.610$^-$22J, we can estimate decoherence time due to linewidth broadening as:

$$\gamma = \frac{linewidth * 1meV}{2\hbar} \tag{4.20}$$

Input electric field dependent Rabi frequency can be written as:

$$\Omega_{Rabi}(Power) = \frac{\mu E_{field}(Power)}{\hbar} \tag{4.21}$$

and $\chi = \frac{\Omega_{Rabi}}{2}$ From equation 4.16 and 4.17, considring resonant condition i.e. δ=0, we can find excited state population and Intensity count as function of linewidth:

Figure 4.3 represents variation of excited state when excied by laser of 400nm wavelength and 1uW input power, and considering 6% radiative recombinaion efficiency[12]. Linewidth unit along x axis is in meV. Further, figure 4.4 represents variation of emitted intensity as function of linewidth, for a given excited input power of 1uW.

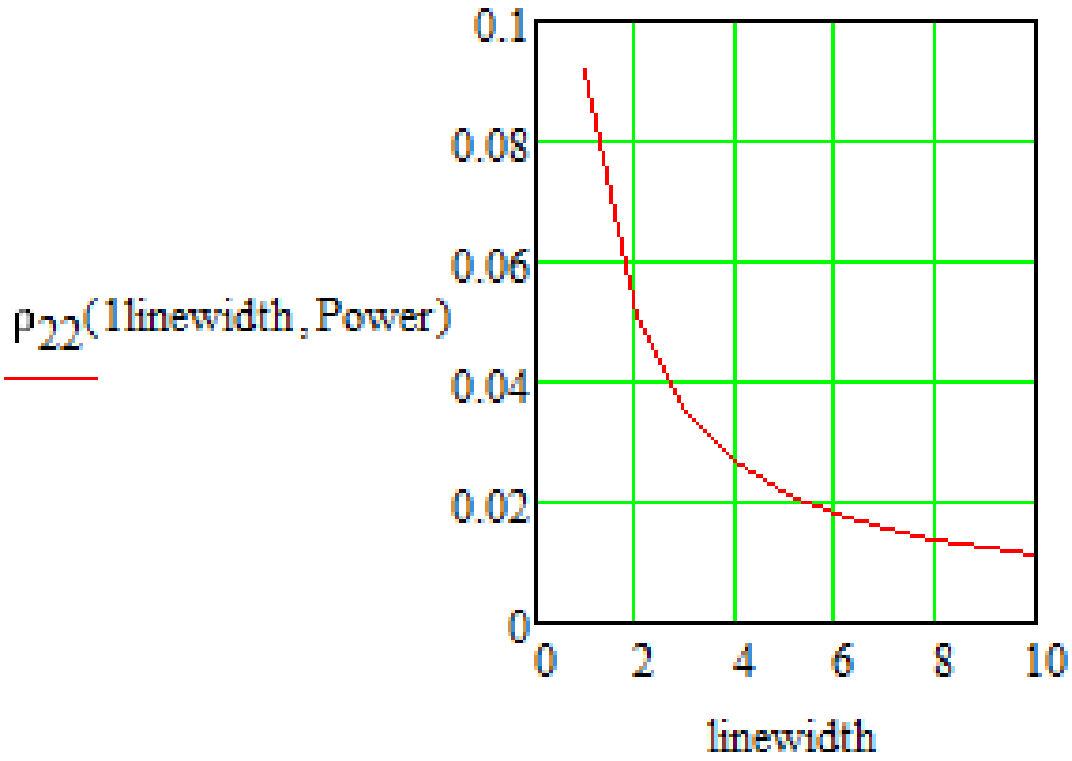

Figure 4.3: Variation of excited state population in GaN based quantum dot as a function of linewidth for input excitation power of 1 uW. Linewidth in meV.

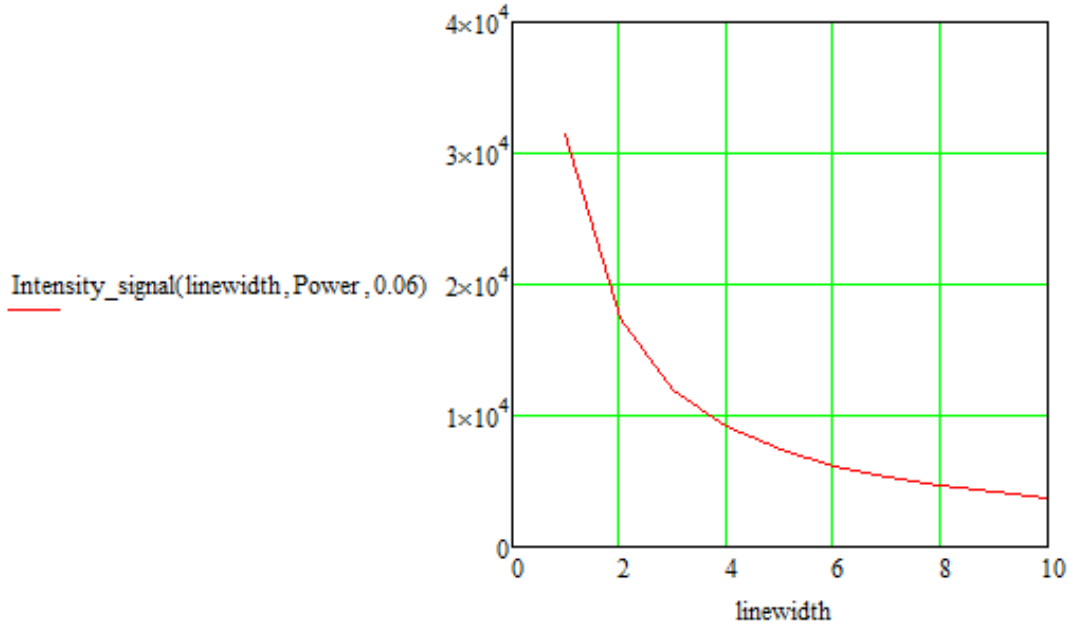

Figure 4.4: Variation of emitted intensity in GaN based quantum dot as function of linewidth for input excitation power of 1 uW, and considering radiative recombination of 6%. Linewidth in meV.

From the figure 4.4, it can be estimated that peak emission at resonance is around 3775 cps for 10meV of linewidth and excitation power of 1uW i.e. $2x10^{12}$ photon counts. In chapter 5 we discuss the experimental setup that has suppression of $10^{-}9$. So, we can achieve signal to noise ration of over 1 i.e. it is possible to observe resonance fluorescence in GaN under above mentioned conditions. For the quantum dot discussed in[12], excited state decay time is 1ns i.e. excited state decay rate γ=1000MHz. On similar lines, we have estimated the intensity of emission at resonance in GaAs based quantum dot.

Estimation is based on details discussed in [11]. For GaAs, we have considered dipole moment of 25D, 200nW of excitation power, 100% radiative recombinaion efficiency. Then at resonance, we expect emission intensity as shown in figure 4.6.

This estimation for GaAs was compared with the experimental result obtained

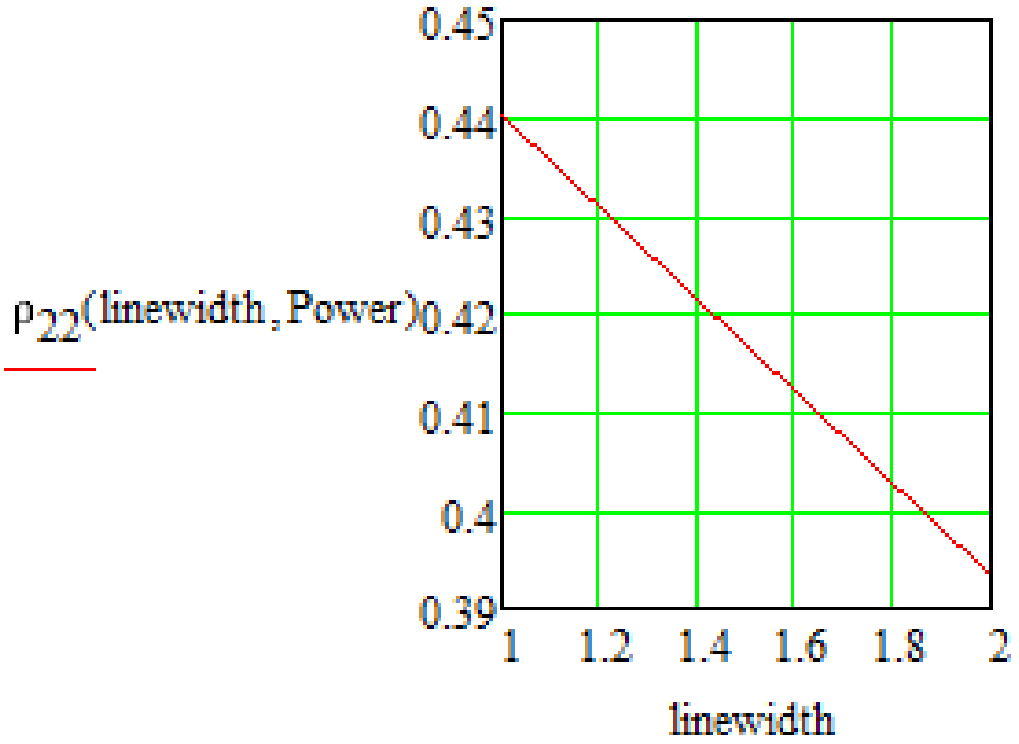

Figure 4.5: Variation of excited state population in GaAs based quantum dot as function of linewidth for input excitation power of 200nW, and considering radiative recombination of 100%. Linewidth in ueV.

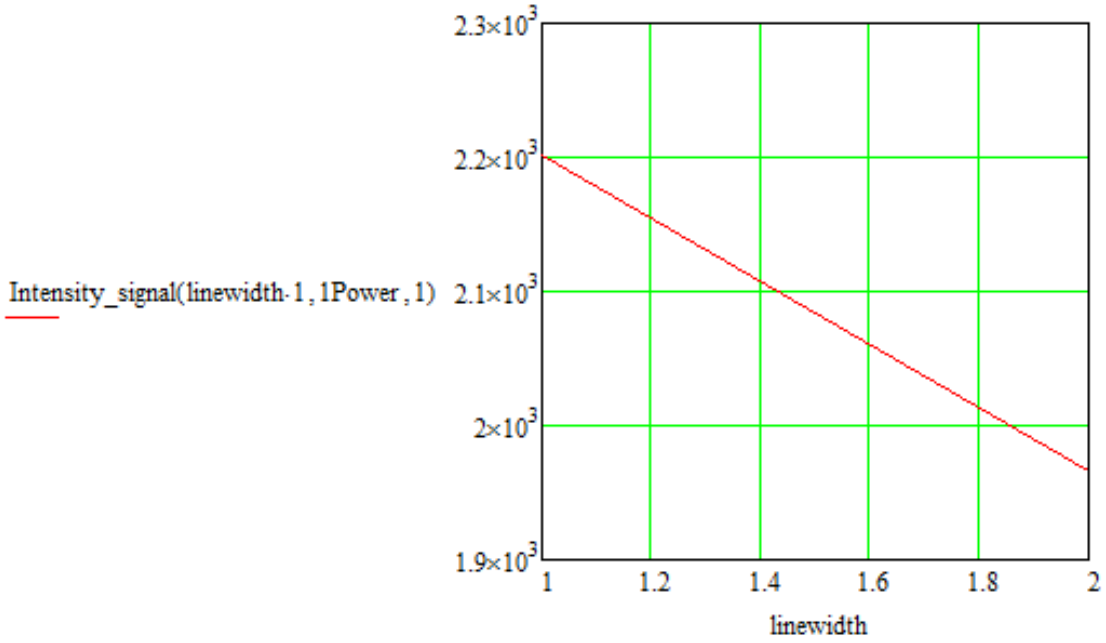

Figure 4.6: Variation of excited state population in GaAs based quantum dot as function of linewidth for input excitation power of 200nW, and considering radiative recombination of 100%. Linewidth in ueV.

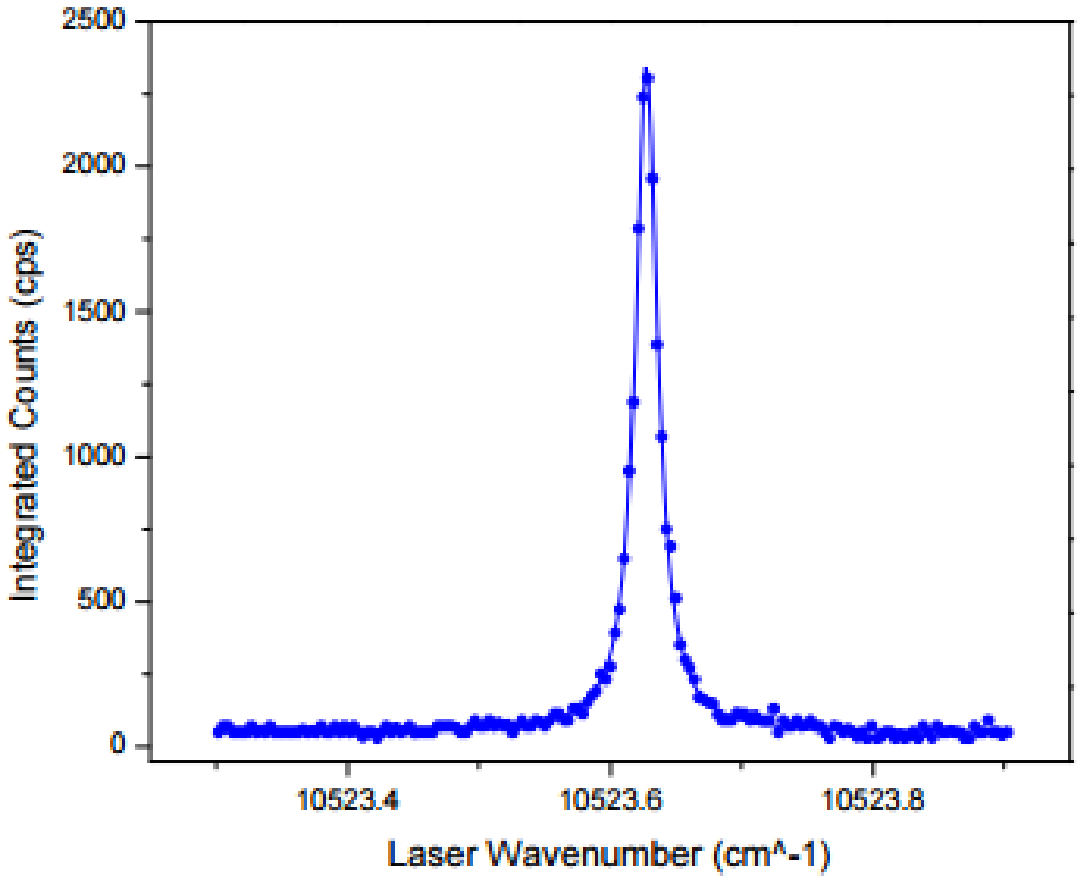

Figure 4.7: Measured resonance fluorescence intensity in GaAs quantum dot trion state[11].

in [11]. On comparing counts on resonance between figure 4.6 and 4.7, we estimate linewidth from figure 4.6 for GaAs quantum dot to be around 1ueV which holds true from figure 4.7.

4.4 Summary

Phenomena of resonance fluorescence is explained. Further spectrum for resonance fluorescence is derived in two-level system. Finally, we estimate intensity counts in GaN and GaAs based quantum dots.

CHAPTER V

Experimental study of Resonance Fluorescence in WSe2 monolayer sample

This chapter mainly deals with describing experimental setup and techniques to perform resonant fluorescence spectroscopy in WSe_2 monolayer sample. We then describe our results and look into theoretical details of resonance fluorescence signal in WSe2 monolayer quantum well by considering it as three level system.

5.1 Experimental setup

Figure 5.1 shows block diagram representation of the reflection based experimental setup for the study of resonance fluorescence. We are using CW Ti:Saphire SolTis laser for exciting the sample. The laser is input to the setup through a single mode fiber. We use continuous ND filter to control the excitation power. Input laser is polarized to H or V using glan thompson polarizer. Before exciting the sample through a beam splitter and an objective lens, the beam is expanded. Reflected beam from the sample and emission is collected through collection arm that consists of W1, quarter waveplate to eliminate ellipticity introduced due to birefringence in optics. W2, quarter waveplate is used to rotate the polarization of the analyzing polarizer. To create cross polarization condition in the setup we don't rotate polarizer as it shifts the beam outgoing into the single mode fiber at the collection port to the

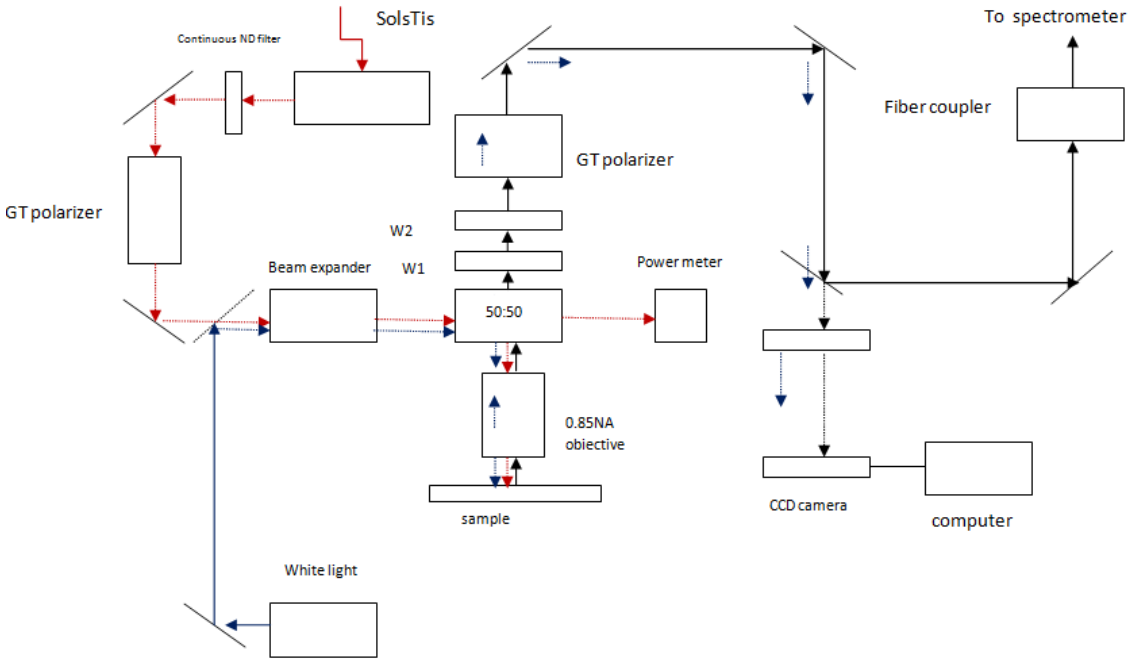

Figure 5.1: Experimental setup to study Resonance fluorescence in TMDC material

spectrometer. White light image (show in blue dash line) is obtained on the CCD camera. The red arrow represents excitation laser, and the black arrow represents path of emission from the sample. One of the major challenges in the experiment is to suppress the background laser. We have achieved the suppression by using cross polarization technique in association with confocal rejection of the scattered laser by using a single mode fiber as a coherent detector.

5.2 Polarization dependent beam deformation in resonant fluorescence setup

In normal incidence setup beam spot smaller than that in angular excitation setup. Consequently, less power is required to obtain the given excitation intensity. In addition, unlike in angular excitation setup where the scattered beam is more likely to be un-polarized, in normal incidence setup scattered beam from diffraction limited focused beam spot is polarized. Consequently, this polarized scattering can

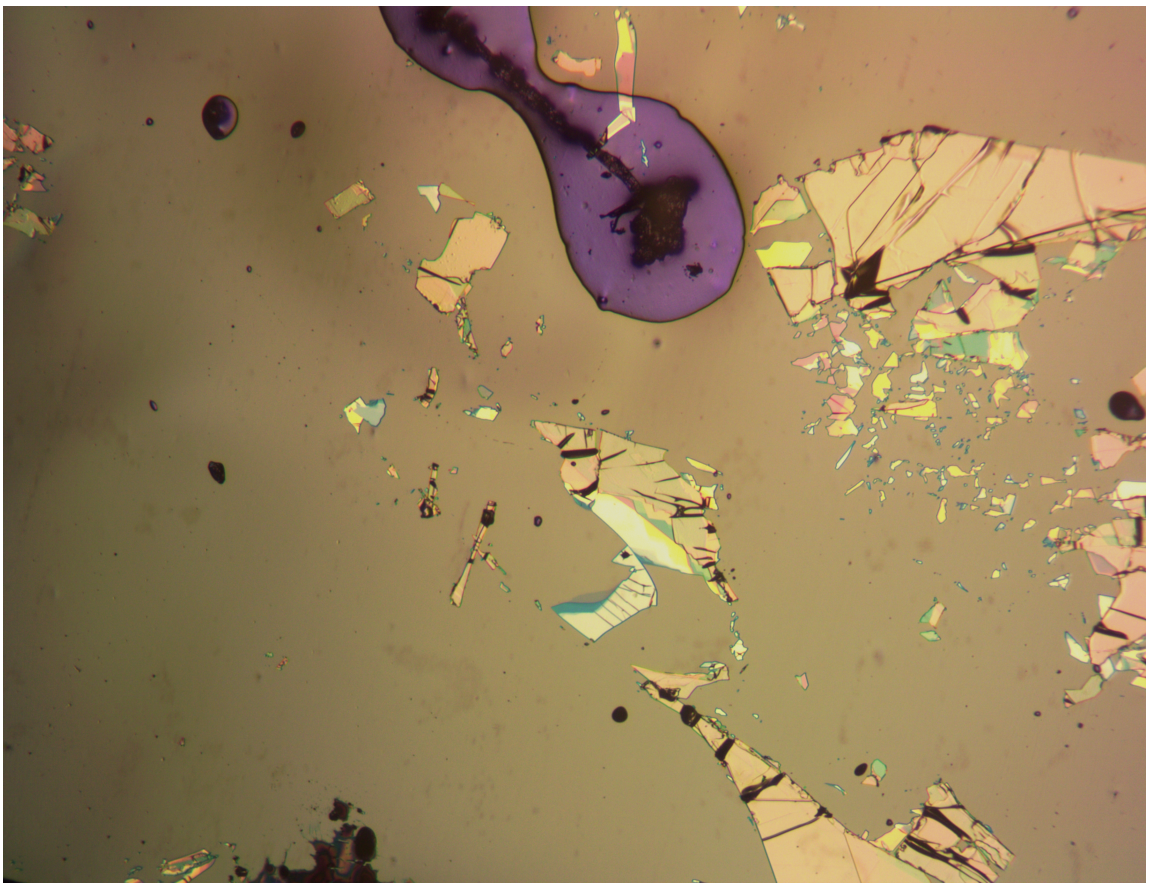

Figure 5.2: Microscope image of WSe2 Monolayer sample 5X magnification(sample prepared by Timothy Chou)

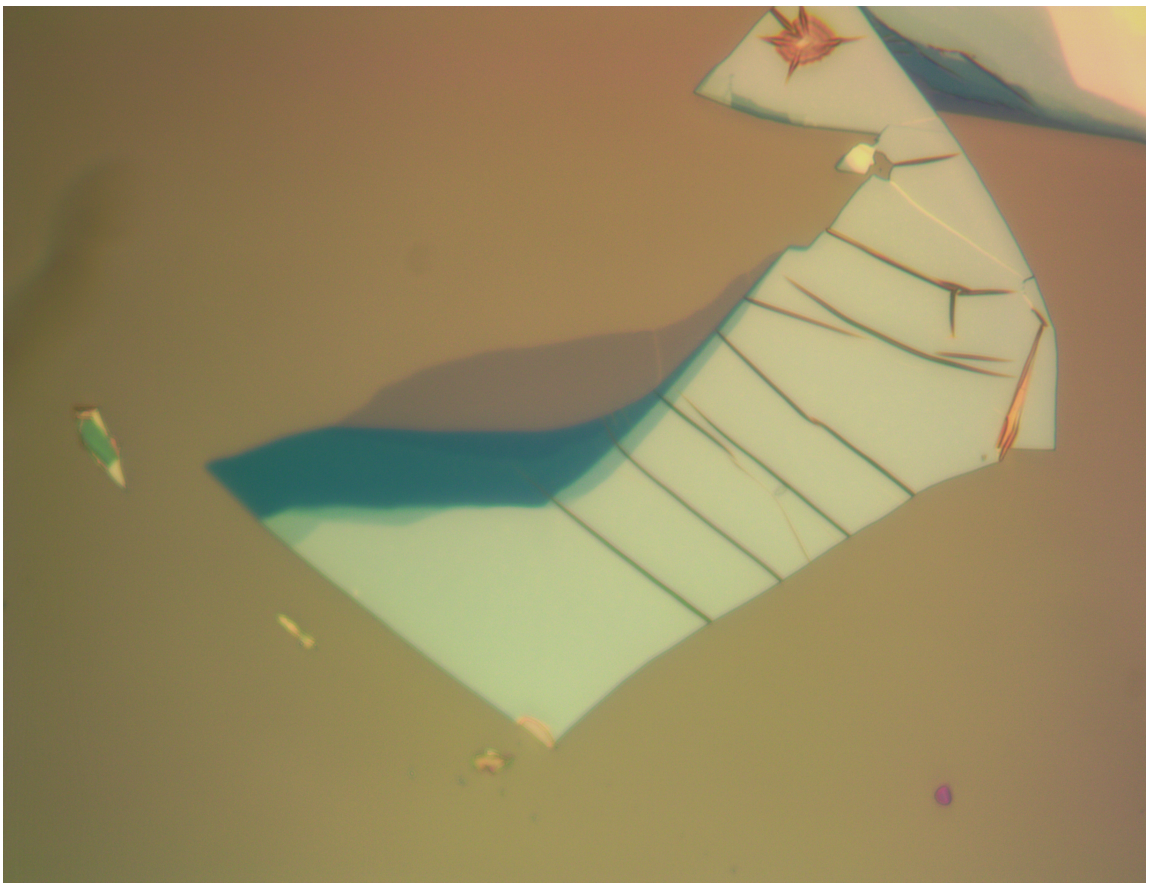

Figure 5.3: Microscope image of WSe2 Monolayer sample 40X magnification(sample prepared by Timothy Chou)

form interference pattern that further suppresses excitation laser. Care must be taken to obtain diffraction limited beam spot size in order to observe the interference pattern when an objective lens in placed between a pair of crossed polarizers.

In the collection arm of the setup, laser scattered from the sample surface is collimated to quarter waveplate which removes any birefringence introduced by the excitation optics. Further, half wave plate together with Glan Thomson GTH10A as an analyzer creates cross polarization for the excitation laser. While in the excitation arm, a single mode fiber is the source of excitation laser (coherent illumination). This single mode fiber can be considered as circular aperture, and when focused it results in point spread function, as shown in figure [40], in the form of airy disk pattern whose intensity can be described in terms of Bessel function[40]. Intensity pattern above can be obtained by integrating over wavefront in the pupil for any given point in 3D [40] which defines the confocal volume which is same as the observation volume in confocal imaging in normal incidence setup. So, the confocal volume observed in the confocal plane is simply product of both the respective psf. Alternatively, each of these psf can be understood as probability of photon into the volume and probability of receiving the photon from this volume into the confocal plane. So, if we use a single mode fiber for detection, we need to convolve psf and pinhole. Mathematically, it is just convolution of two psf and multiplying with pinhole [40]. The idea behind using confocal technique is that it has better resolution than wide field microscopy and convolved psf is sharper. So, we have less contribution in background noise as side lobe of the diffraction pattern is not present in the confocal function. In diffraction pattern formed by a confocal system, we have less energy in outer lobe than in the pattern formed by a single lens which has diffraction pattern described by airy function[40]. Also, size of pinhole matters. Image of pinhole in focal plane

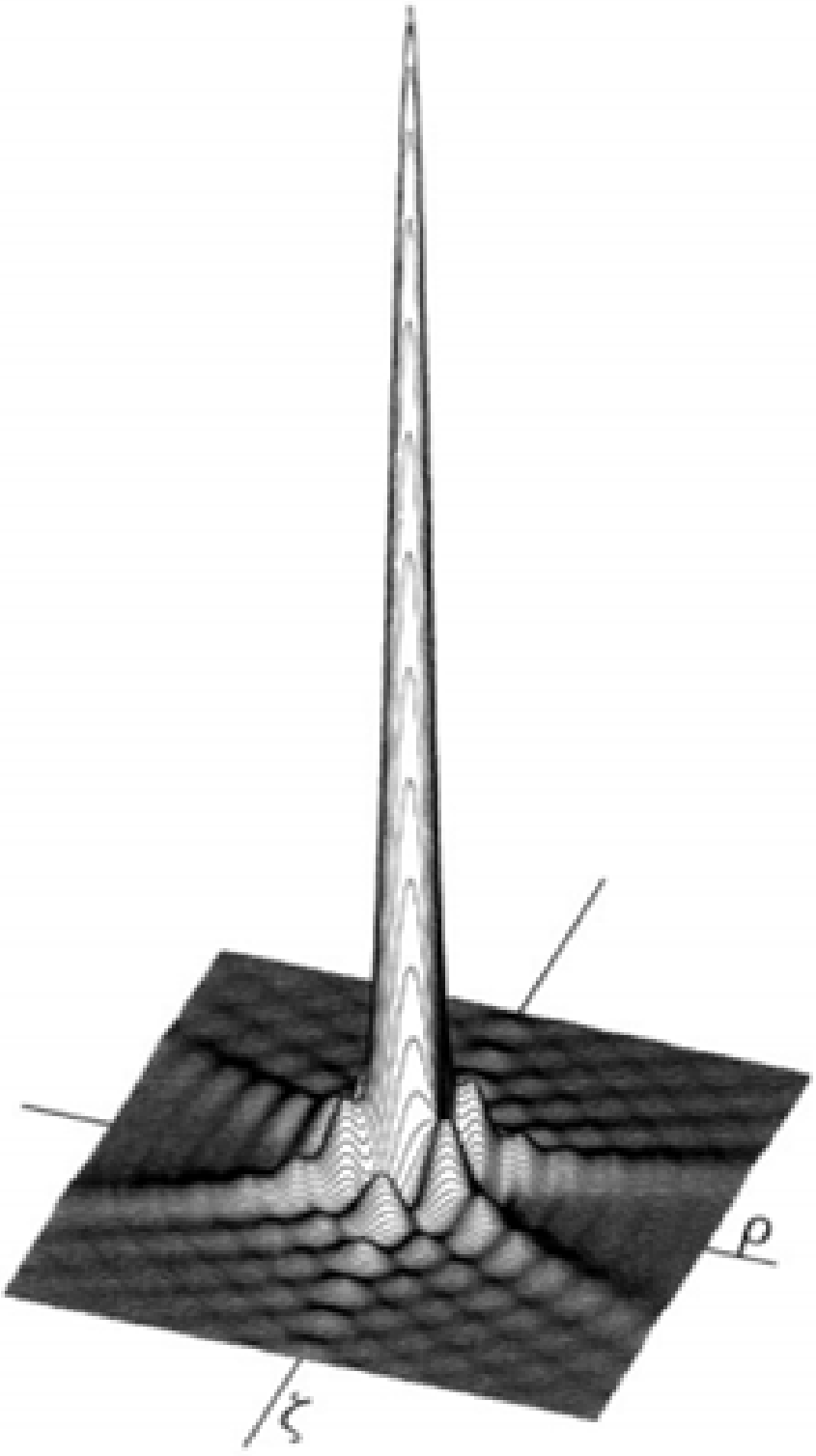

Figure 5.4: Point spread function of circular aperture in focal plane [40]

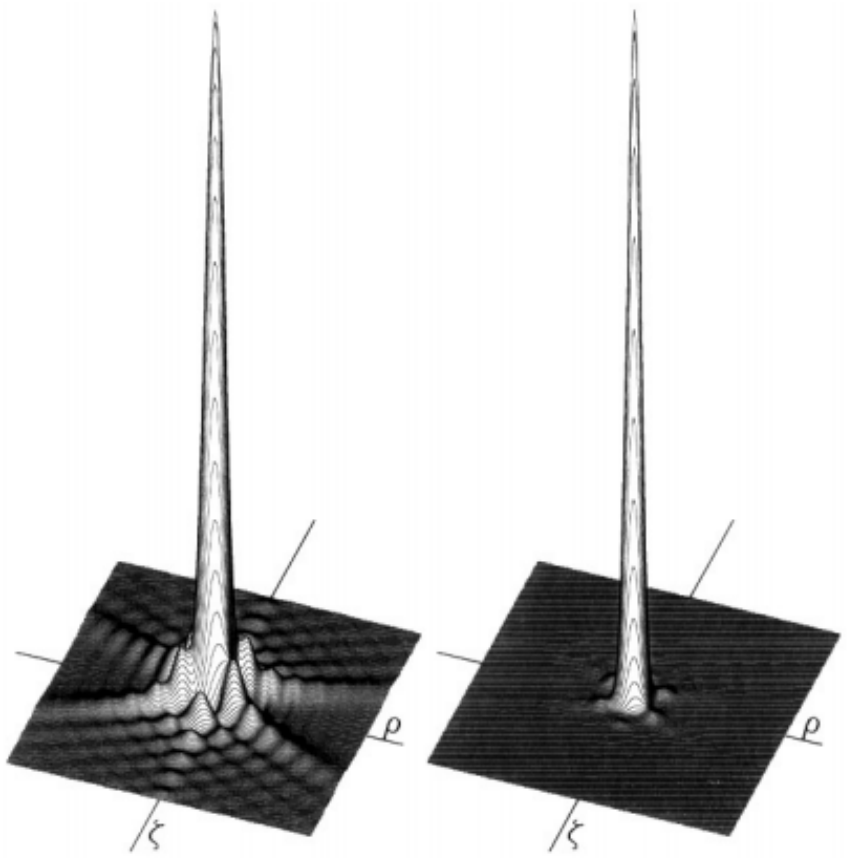

Figure 5.5: : Diagram showing absence of side lobe in diffraction pattern in confocal microscopy [40].

denotes the area from which photons will be collected. Any size less than 1 AU will result in signal loss. So, the selected pinhole size should be near 1AU. Pinhole determines focal volume on the sample surface. If source and detector pinholes are large, we approach widefield limit. When using pinhole in confocal system, "lateral improvement is much more sensitive to the pinhole size than the axial resolution. So, changing the NA of fiber launching lens is same as change in pinhole size". So, we can use either multimode fiber or a single mode fiber as detector. However, usage of a single mode fiber has its own advantage[41].

In case of a "single mode fiber as detector, the detected field is the overlap integral between field at the input of the fiber and the mode pattern"[41]. Propagation of modes in optical fiber has been studied in[42].

$$E_t = \sum_p a(p) * e(p) \qquad H_t = \sum_p a(p) * h(p) \tag{5.1}$$

for pth mode. Where excitation efficiency of the pth mode:

$$a(p) = \int e(p) x h(q) * z dA \tag{5.2}$$

is 0 if p≠q, and 1 if p=q.

i.e. overlap integral determines extent of propagation of the transverse wave in the fiber. Moreover, detected intensity = $|a_p|^2$

For fundamental mode: $I_1 = |\int \int_{-\infty}^{\infty} E * e_1 ds|^2$

Consequently, excitation efficiency of the given mode reduces with the value of overlap integral. Based on this idea, we tried to reduce the overlap integral by deforming the mode of the beam input to the single mode fiber. Apart from using con-focal rejection, we also used polarization microscopic technique. Since coupling of mode into a single mode fiber depends upon overlap integral, we found that diffraction image in polarized microscopy is not Gaussian but an interference pattern in the

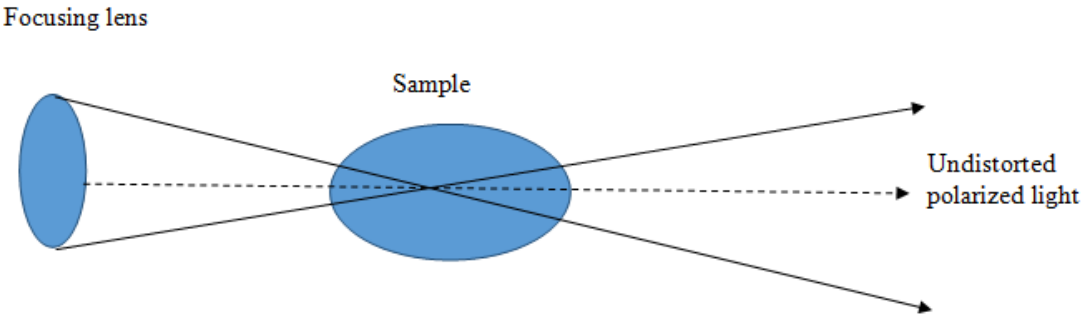

Figure 5.6: : Formation of Maltese pattern due to birefringent sample.

form of Maltese pattern. Consequently, coupling of background noise can be further reduced as overlap integral of the diffraction image with a single mode fiber is less. These interference patterns or Maltese pattern is generated due to polarization aberration. These aberrations can occur either due to interaction of optical wavefronts and surface of lens. Here, diverging beam incidents obliquely to the surface of the lens along the edge has different Fresnel reflection coefficient for S and P polarization. Consequently, we have rotation in the polarization state. Or it can be obtained when a polarized beam is focused on a birefringent material like a sample or half ball lens where polarization state of the beam is distorted. Birefringent sample is one of the common sources of interference pattern in polarization microscopy. When polarized excitation laser is focused on a birefringent sample, polarization of transmitted along the optical axis remains unchanged. However, due to birefringence of the sample, polarization of the off axis transmitted light is distorted. So, when an analyzer is placed in crossed configuration w.r.t polarizer, light along the optical axis gets extinguished, but those towards periphery, passes through orthogonal forming an interference pattern.

Formation of an interference pattern in birefringent sample is shown in the diagram below: Figure 5.7 represents interference patterns in different minerals. These

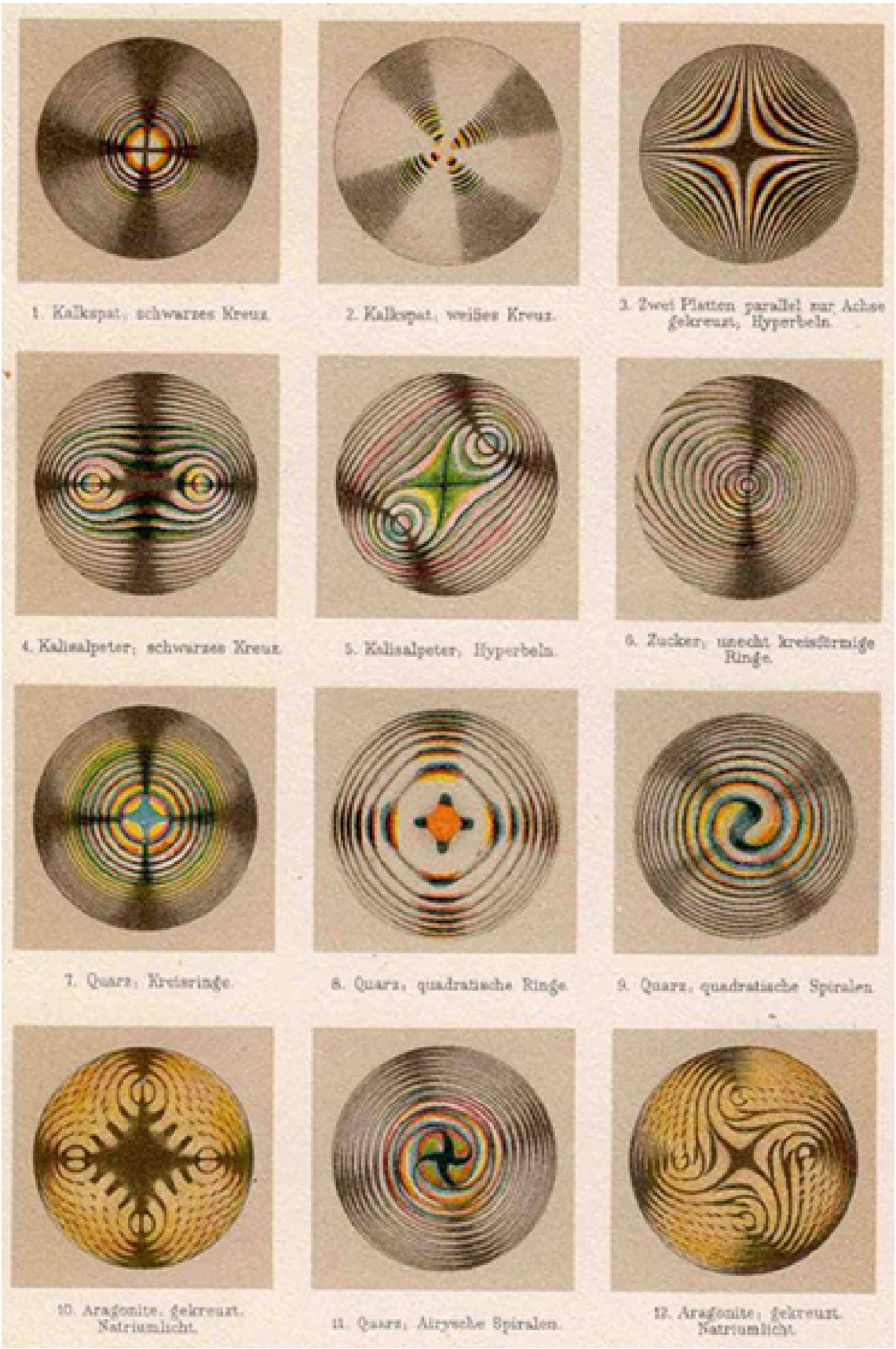

Figure 5.7: : Chromolithograph of optical interferences[43].

patterns are used to characterize minerals based on their composition. Moreover, the interference pattern in bi-axial minerals is shown in the figure 5.8.

Inorder to understand the source by which we can generate such interference pattern in our setup, we used birefringent waveplate as a test sample. Figure 5.8 and 5.9 represents the interference pattern observed by using the birefringent waveplate.

From figure 5.10 and 5.11, it was understood that birefringence is one of the important factors in the formation of such an interference pattern. However,the central portion of the pattern is still not completely extinguished. Consequently, this would result in coupling of scattered background laser in the detector. In order to overcome this, we searched for other sources that can be used to introduce such polarization aberation.

From the diagram 5.12, it is clear that incident beam striking the curved surface of the objective lens is obliquely incident along the periphery. Each of these can be resolved in perpendicular and parallel components. These two vectors have a different reflection. Consequently, an effective vector of the transmitted beam results in rotation in the polarization of the incident beam. As obvious from the Fresnel equation, the component normal to the plane of incident has more reflection. The extent to which rotation will occur has been studied in [44].

It is due to this polarization aberration, either due to birefringence nature of the sample because of varying retardation of converging/diverging light source or rotation on the curved surface of the high NA lens that results in four bright quadrants separated by the dark cross as shown in the figure below. The two respective dark arms are called Isogyres and the central region where Isogyres intersects are called melatope. Mathematical analysis of the formation of such structures has been extensively studied in [45]. In polarization microscopy, lenses produce rotation in plane of

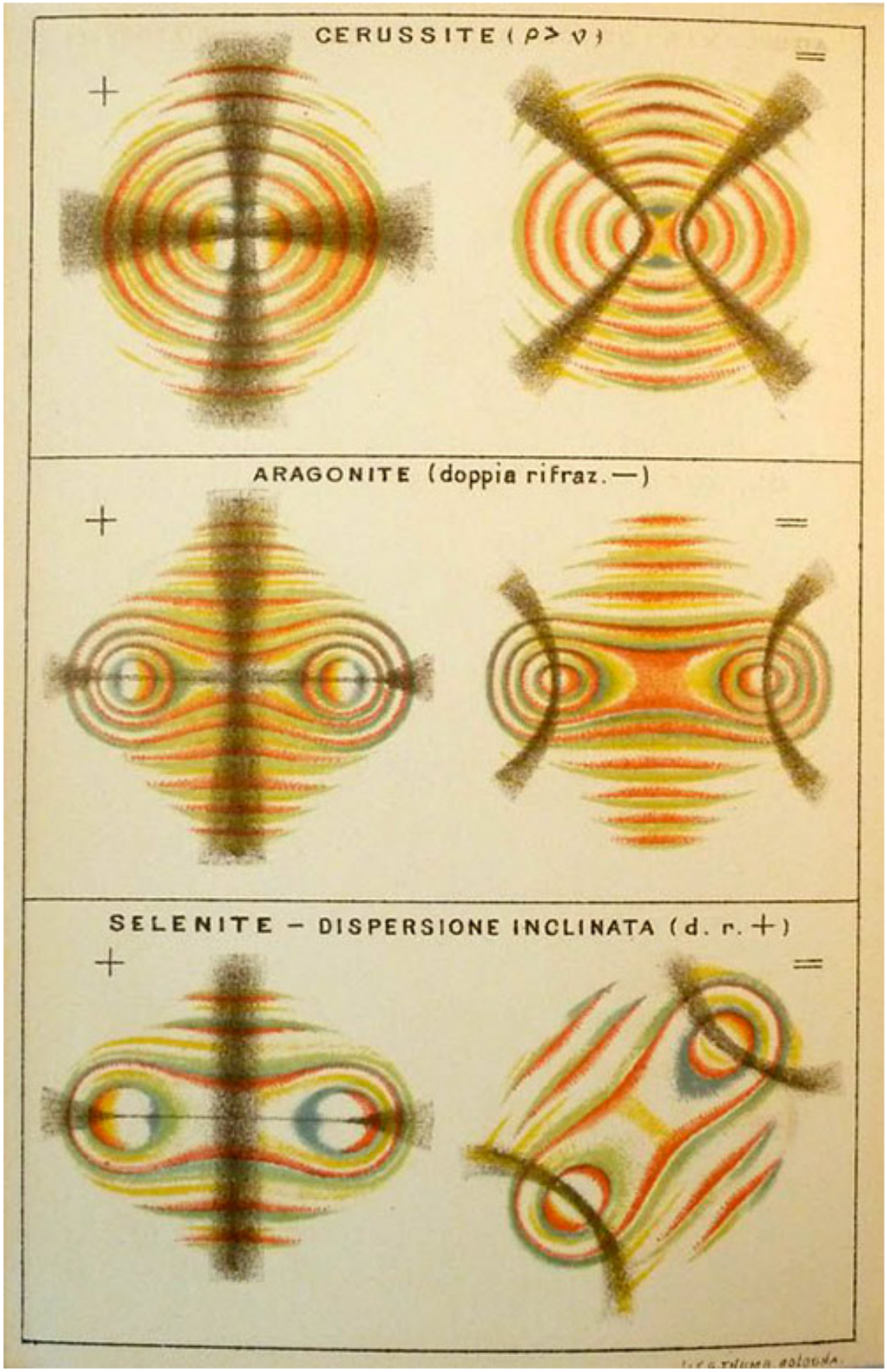

Figure 5.8: : Optical interferences in bi-axial crystals;Bombicci Porta [1889].

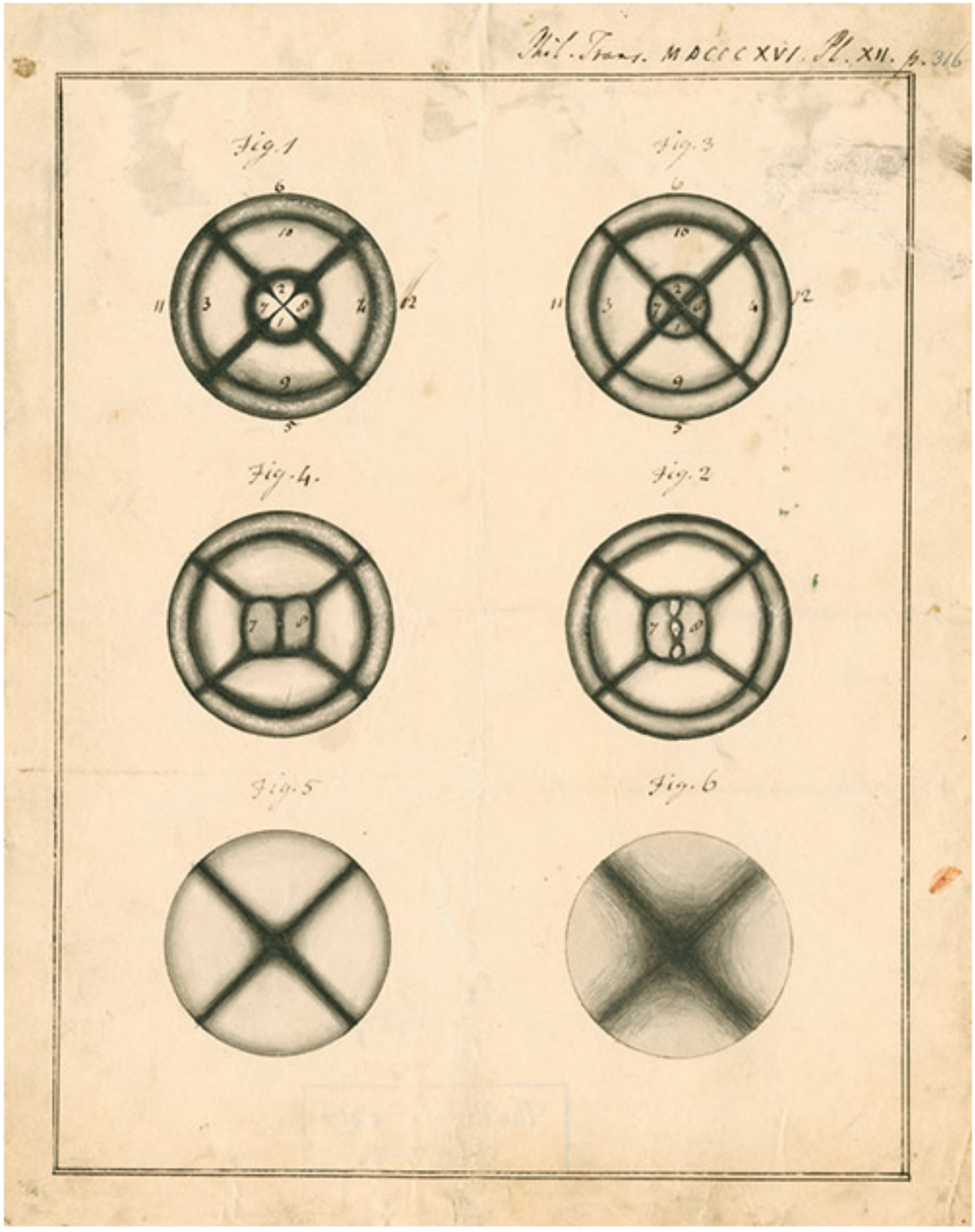

Figure 5.9: : Optical interference effect during heat treatment of glass, David Brewster, 1815.

Figure 5.10: :Maltese like pattern obtained with 532nm laser.

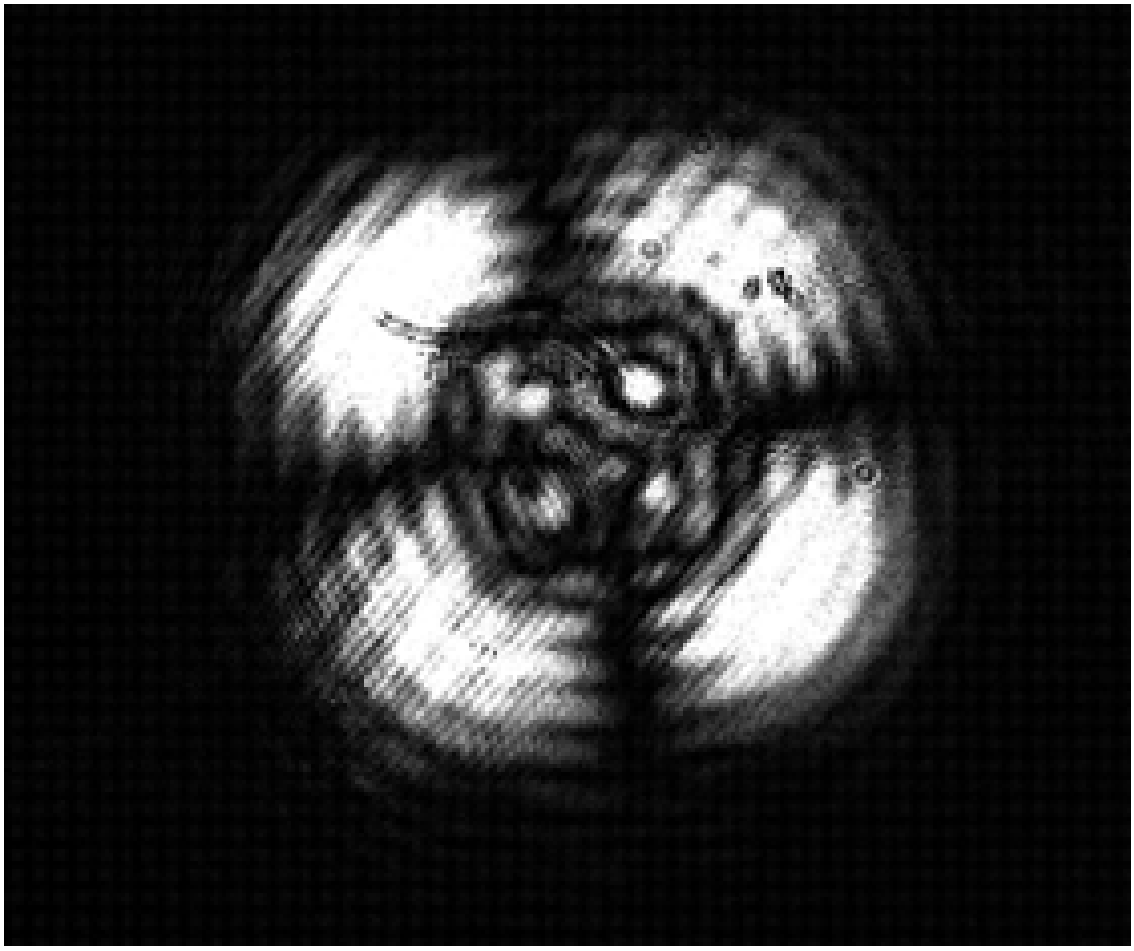

Figure 5.11: :Maltese like pattern on camera.

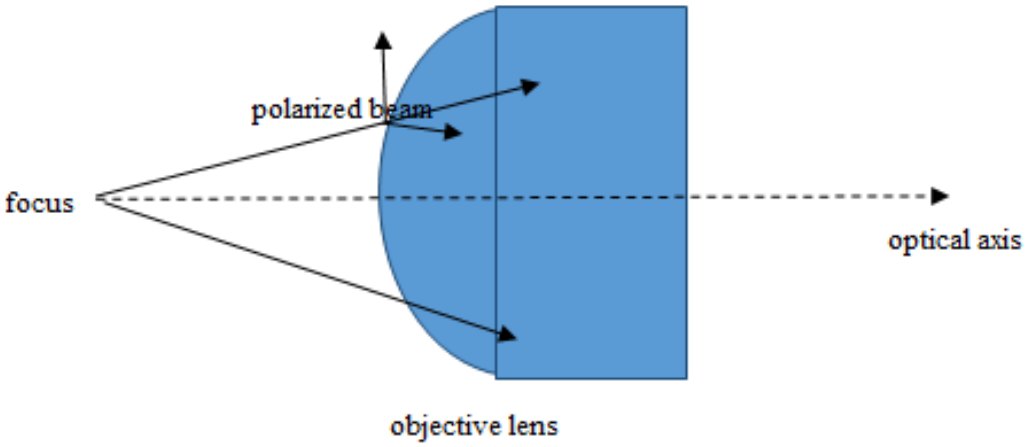

Figure 5.12: :Formation of Maltese structure in reflection setup.

polarization due to difference in Fresnel coefficient for s and p polarized components of the excitation laser[46]. "If amplitude of light in the exit pupil of an objective lens is P(ρ, ϕ), then the amplitude of the image in conjugate plane is given as the Fourier transform of P(ρ, ϕ):

$$A(r,\theta) = \int_0^a \int_0^{2\pi} P(\rho,\phi) e^{iz\rho cos(\theta-\phi)\rho} d\rho d\phi \tag{5.3}$$

(r, θ) and (ρ, ϕ) are the polar coordinates of the exit pupil and in image plane, a is the radius of the exit pupil, and $z = \dfrac{2\pi r}{\lambda * l}$ where l is distance between exit pupil and image plane"[46]. It has been shown in [46] that the intensity distribution as derived using circle polynomials, take the form of airy disk. Assuming ideal objective lens, in cross polarized configuration, A can be expressed in terms of $sin2\theta$ form[46]. So, for theta = 0 and 90, Intensity = 0. So, we have light coming from four different quadrants. In order to satisfy the above relation, "the light in four alternate zones are phase shifted to interfere destructively and give dark cross"[46]. Mathematically, we can write the intensity distribution in terms of Bessel function as[46]:

$$I = const * \sin^2(\theta) \frac{J_3(az)^2}{a^2 z^2} \tag{5.4}$$

Initially we had argued that it is the nature of the sample, like uni-axial structure, which results in formation of such structures. It was observed that origin of so called Maltese structure has same mathematical representation. This explains why we can obtain Maltese structure by two different techniques.

Figure 5.14, 5.15 and 5.16 represents 2D pixel plot and 3D of the Maltese pattern generated in the setup respectively. It is important to note that inorder to reject the background laser, we must suppress the central region of the pattern.This dark region is also called melatope. Consequently, this beam deformation reduces overlap integral between mode pattern and detected field, resulting in rejection of excitation

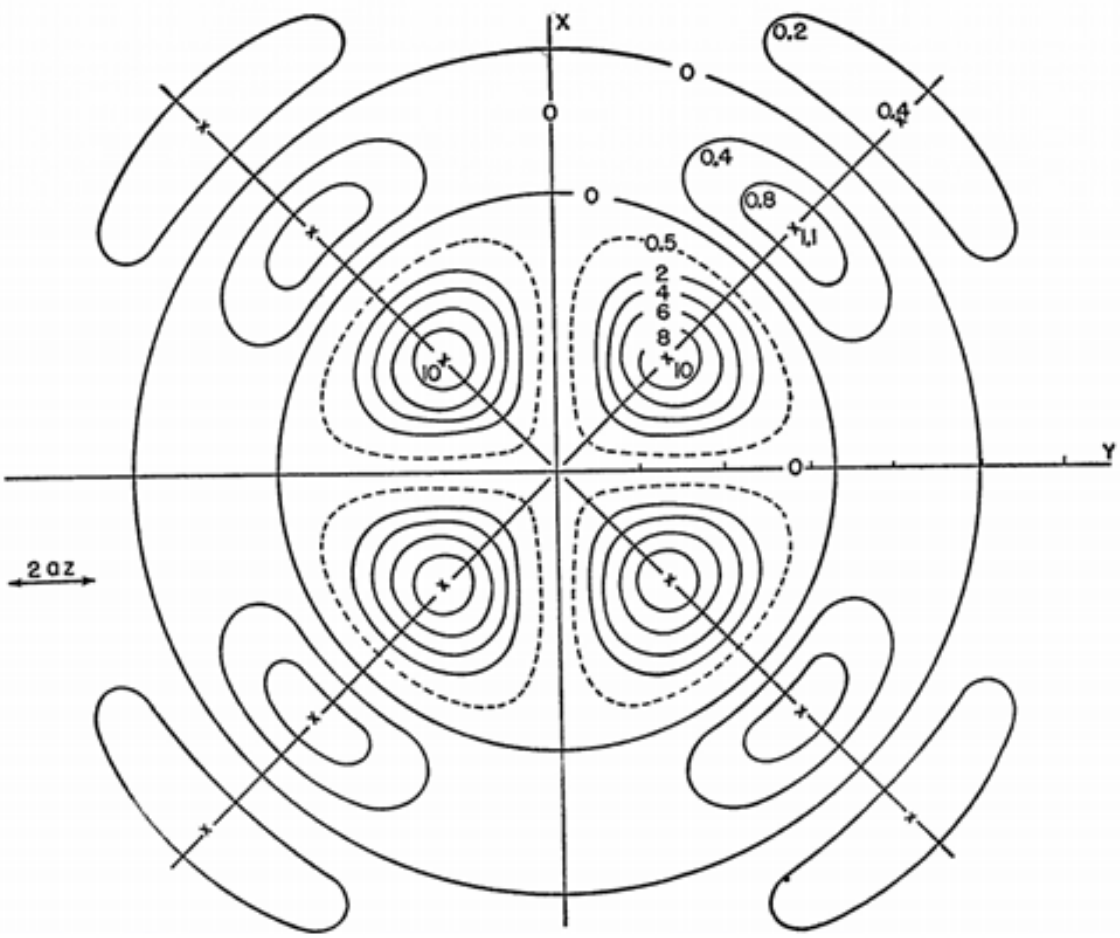

Figure 5.13: : Contour map of Maltese pattern formed in polarization microscopy [46].

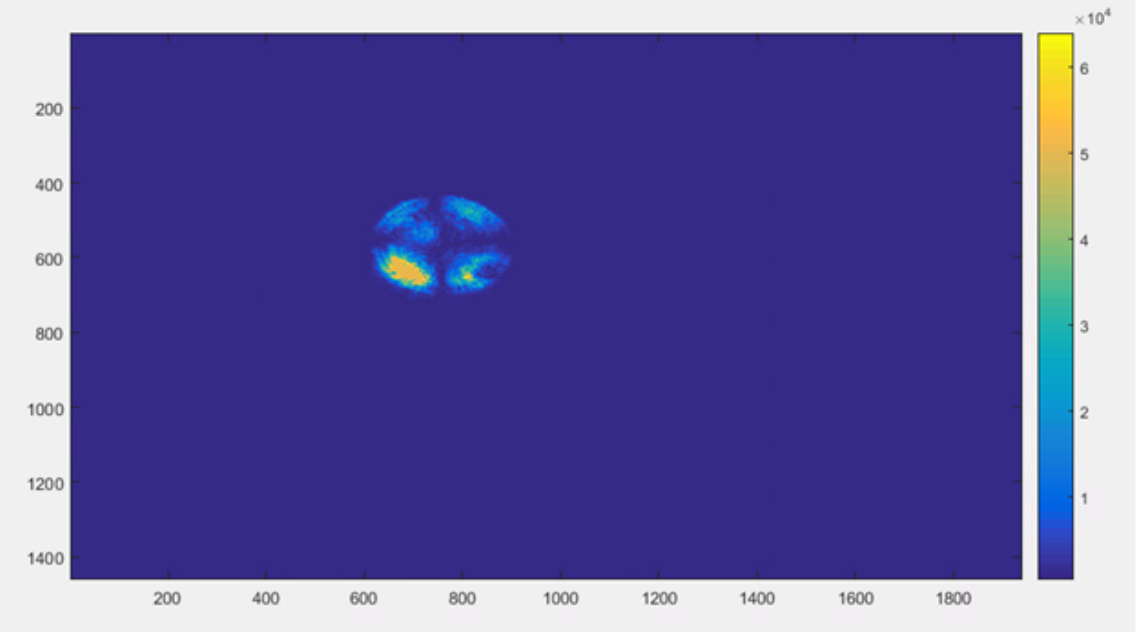

Figure 5.14: : Maltese pattern generated in the setup.

laser.

5.3 Results

In this section, we discuss the resonance fluorescence measurement in the setup shown in figure 5.1. As a first step towards measuring the resonance fluorescence, we obtained emission profile from photoluminescence excitation where the sample was excited with energy higher than the transition energy.

From the figure 5.17 and 5.18, it can be observed that zero phonon line is located around 745nm, and linewith is approximately 18nm. All measurements have been taken at room temperature.

In the experiment, the excitation laser was linearly polarized by using Glan Thompson polarizer. We used white light setup to locate the monolayer sample. In the next step we made sure to excite the monolayer. Further,the excitation wavelength was fixed at 710nm and optics was aligned to obtain maximum PL emission.

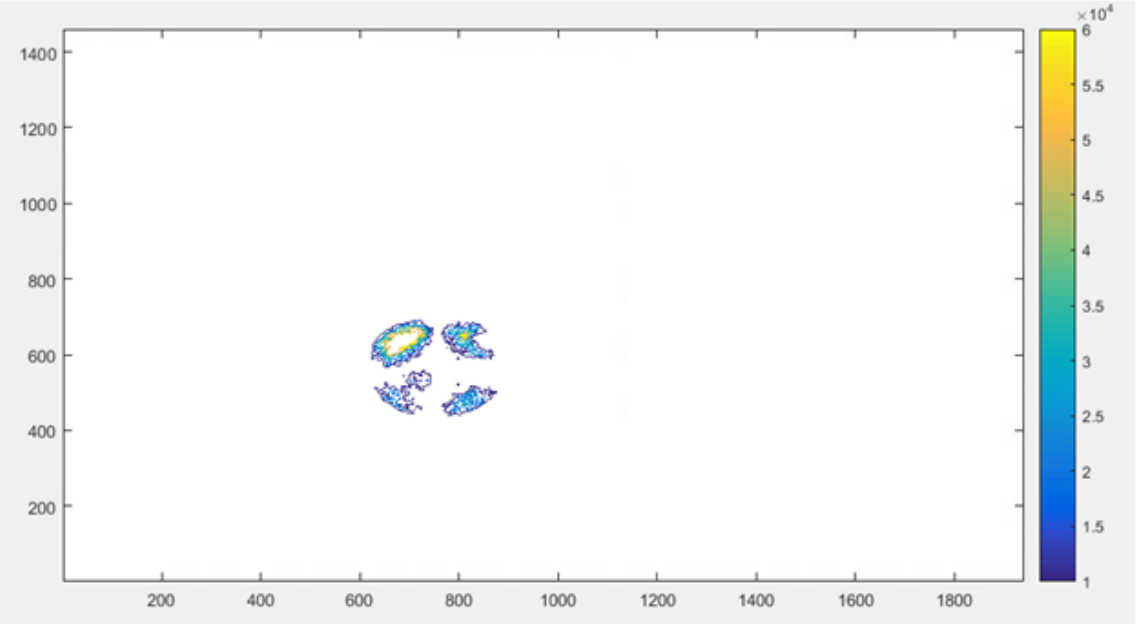

Figure 5.15: : Contour pattern for Maltese generated in the setup.

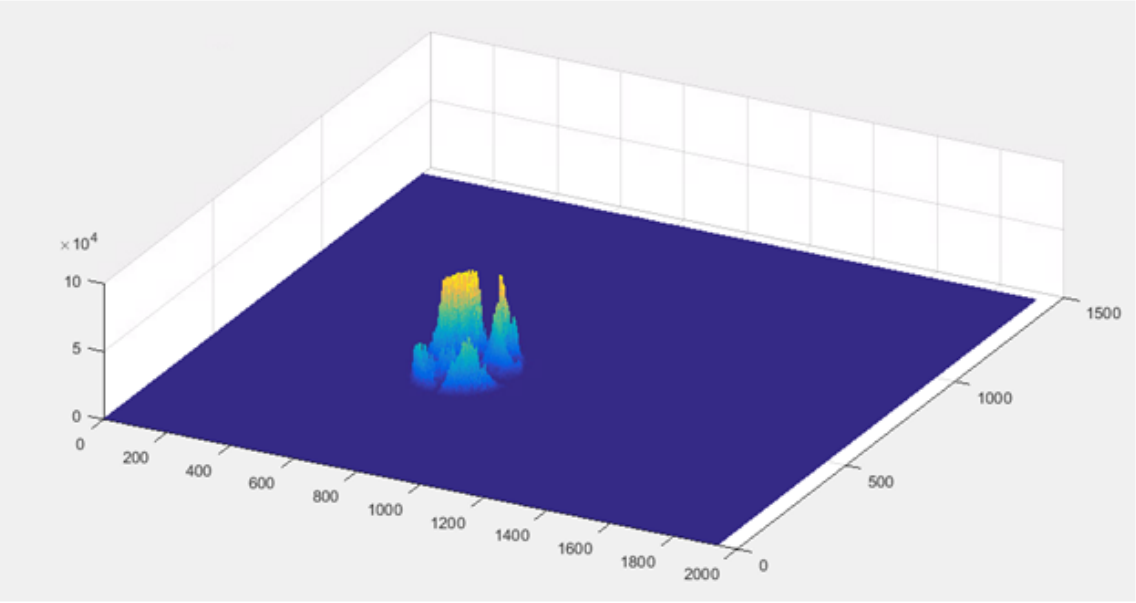

Figure 5.16: :3D Contour pattern for Maltese generated in the setup.

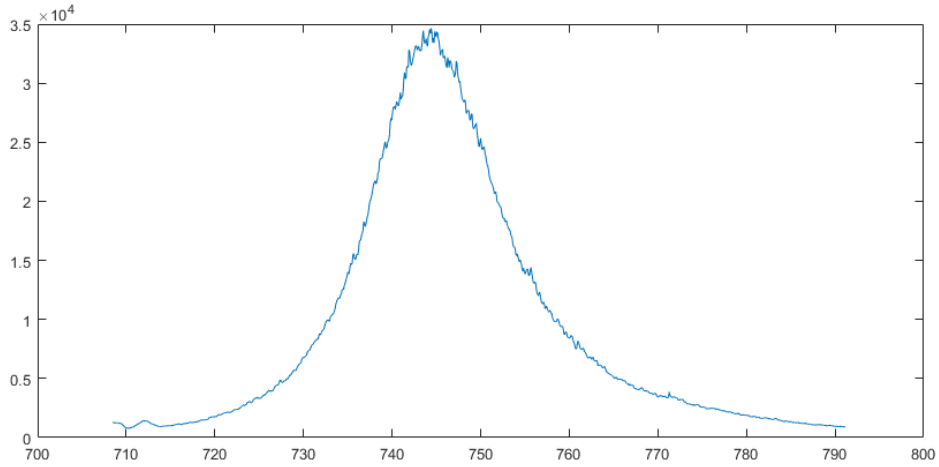

Figure 5.17: :PL profile of WSe_2 sample when excited with 532nm laser, with 24uW of excitation power and 50s integration time.

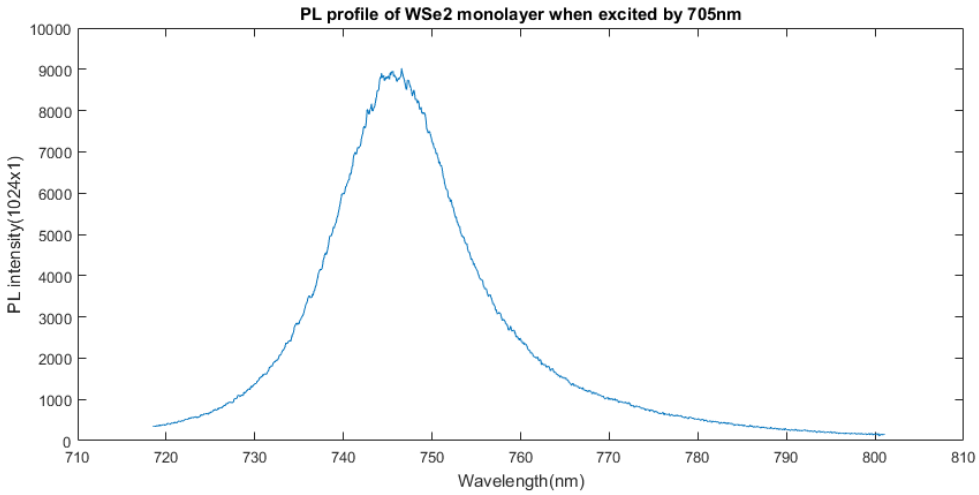

Figure 5.18: :PL profile of WSe_2 sample when excited with 705nm laser, with 90uW of excitation power and 50s integration time.

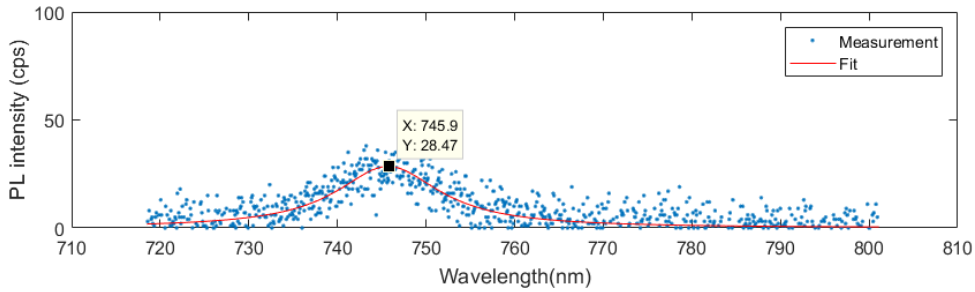

Figure 5.19: :PL profile of WSe_2 sample when excited with 710nm laser, with 25uW of excitation power and 5s integration time.

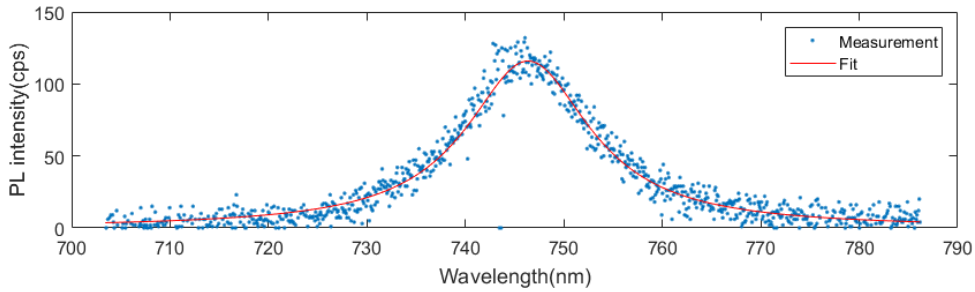

Figure 5.20: :PL profile of WSe_2 sample when excited with 744nm laser, with 25uW of excitation power and 5s integration time.

Once, the setup has been optimized for maximum PL intensity, we optimize the orientation of half waveplate and quarter waveplate to suppress the background laser. This step was repeated for each scan wavelength. We scanned the excitation near the ZPL.

For comparison, figure 5.19, 5.20 and 5.21 represents the experimental and curve fit graph for excitation wavelength of 710nm, 744nm and 760nm respectively.

Figure 5.23 represents variation of integrated counts as function of excitaton wavelength.

Variation of linewidth as a function of excitation wavelength is shown in the figure 5.24. It can be observed that linewidth variation is almost uniform throughout, indicating that the linewidth is mainly homogeneously broadened.

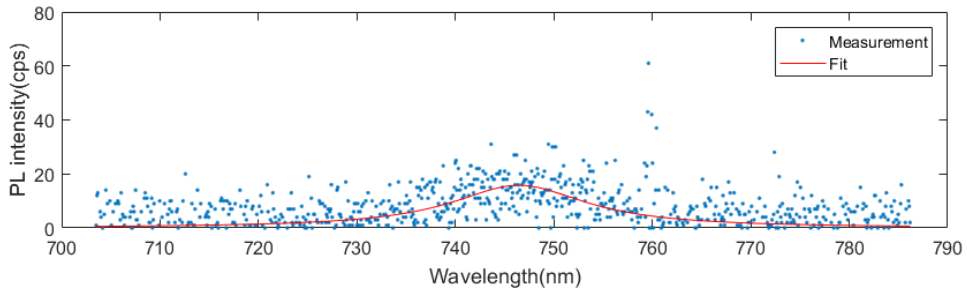

Figure 5.21: :PL profile of WSe_2 sample when excited with 760nm laser, with 25uW of excitation power and 5s integration time.

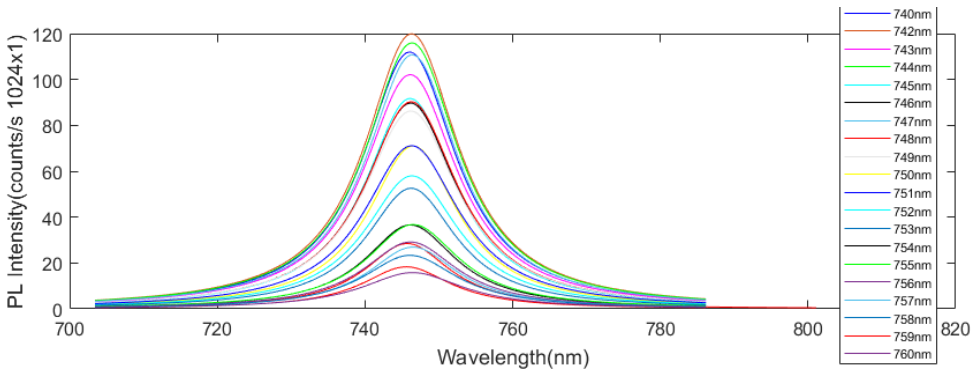

Figure 5.22: :PL profile of WSe_2 sample when excited laser wavelength is scanned from 740nm to 760nm, with 25uW of excitation power and 5s integration time. These are curvefit values.

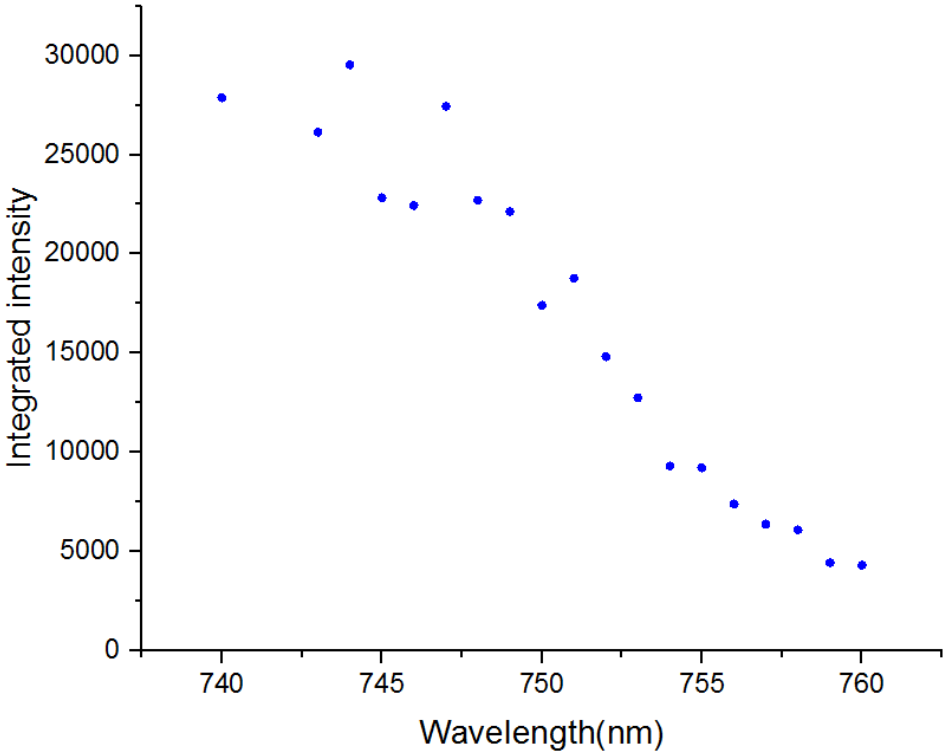

Figure 5.23: :Integrated counts variation as a function of excitation wavelength.

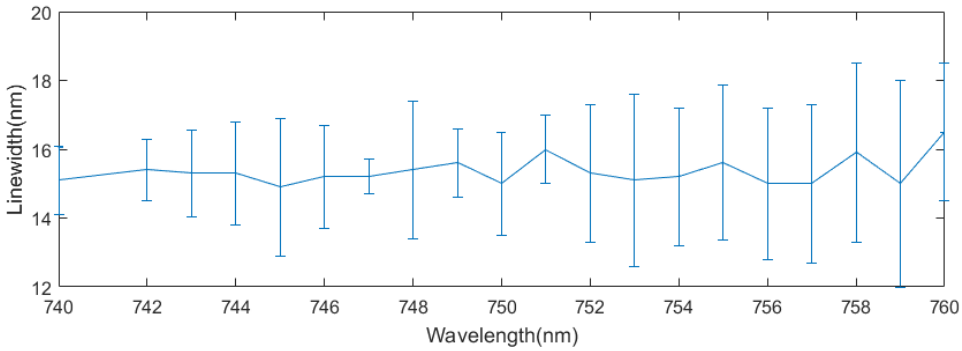

Figure 5.24: :Linewidth variation as a function of excitation wavelength.

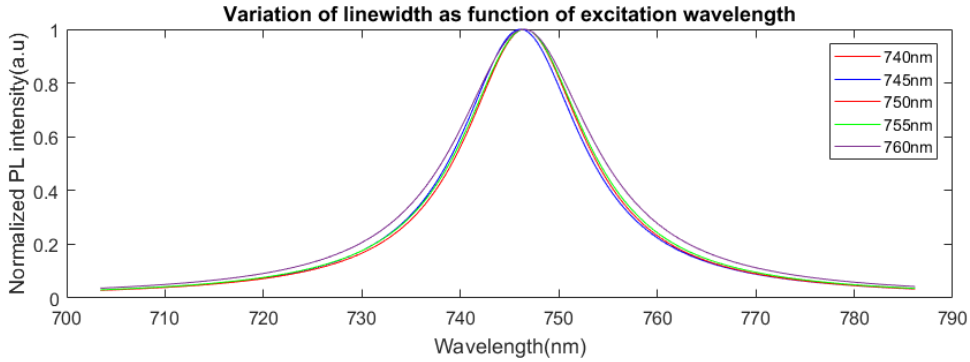

Figure 5.25: :Normalized PL intensity as function of excitation wavelength.

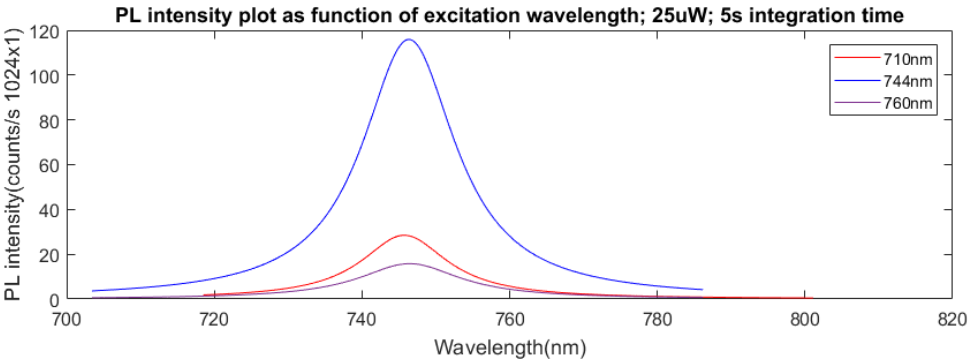

Figure 5.26: :Normalized PL intensity as function of excitation wavelength.

5.4 Theoretical analysis of resonance fluorescence from WSe_2 monolayer sample

Resonance fluorescence in a three level system has been studied by[D Schwedt et al. 2003]. Resonance fluorescence consists of two components: secondary emission and rayleigh scattering. If Γ_1 and Γ_2 represents effective incoherent relaxation rate, then for inhomogeneously broadened ensemble, spectrum is calculated as:

$$I_{||}^{C} = \pi V^2 |\sum_{i=1}^{N} \frac{e^{-i\Delta k(\omega r_i)}}{\gamma - i(\Omega_L - \Omega_i)}|^2 \delta(\omega - \Omega_L) \tag{5.5}$$

$$I_{NC,||} = \sum_{i=1}^{N} \frac{V^2\gamma}{\gamma^2 + (\omega - \Omega_L)^2} \frac{\gamma}{\gamma^2 + (\Omega_L - \Omega_i)^2} [\frac{\Gamma_2 - \Gamma_1}{\Gamma_2\Gamma_1} - \frac{1}{\gamma}] \tag{5.6}$$

$$I_{perp,N} = \sum_{i=1}^{N} \frac{V^2\gamma}{\gamma^2 + (\omega - \Omega_i)^2} \frac{\gamma}{\gamma^2 + (\Omega_L - \Omega_i)^2} \frac{\Gamma_2 - \Gamma_1}{\Gamma_2\Gamma_1} \tag{5.7}$$

Equation 5.5 and 5.6 represents parallel component of resonance fluorescence. The parallel component has coherent part and incoherent part. While perpendicular component has only incoherent part. Coherent part in parallel component has delta behaviour with speckle formation. In our experiment, we have measured the perpendicular component. Parallel component has delta characteristic behaviour due to rayleigh scattering and can be obtained from angular excitation setup.

CHAPTER VI

Conclusion and Future scope

6.1 Conclusion and Future direction

In this thesis, we have discussed fundamentals of low dimensional semiconductors and resonant spectroscopy of such systems. We have also shown the feasibility of observing resonant fluorescence in GaN based quantum dot which has not been reported earlier. Consequently, we can strive towards observing performing resonance fluorescence at higher temperature using GaN based quantum dots. We have also shown resonance fluorescence signal from TMDc material, which is an important step towards TMDC based quantum information application.As a next step, modification in the setup shown in figure 5.1 can be performed to obtain resonance fluorescence signal in GaN and compare the characteristics with theoretical estimation discussed in this thesis. In order to proceed, usage of solid immersion lens is required. Not only it increases the collection efficiency of the emission, but also the excitation beam spot size is smaller. Consequently, less power is needed to realize emission as a function of excitation. Hence better suppression of the scattered laser is expected.

References

[1] B R Mollow, Power Spectrum of Light Scattered by Two-Level Systems, The Physical Review, 1969.

[2] Alice Heather Burrell, High Fidelity Readout of Trapped Ion Qubits, Ph.D. Thesis, Oxford University, 2010.

[3] S.Sun, H. Kim, G.S. Solomon and E.Waks, Cavity-enhanced optical readout of a single solid-state spin, arXiV:170.05582, 2017.

[4] Post-Selectable indistinguishable photons from the resonance fluorescence of a single quantum dot in a microcavity, S. Ates et. al.,Physical Review letters,2009

[5] Site controlled InGaN/GaN single photon emitting diode, Lei Zhang et. al., Appl. Phys. Lett., 2016

[6] Quantum theory, the Church-Turing principle and the universal quantum computer, D Deutsch, Proceeding of the Royal Society A, 1985

[7] A fast quantum mechanical algorithm for database search, Lov Grover, ACM, 1996.

[8] Relativistic Quantum Metrology: Exploiting relativity to improve quantum measurement technologies, Ahmadi et. al., Scientific reports, 2014.

[9] On Optical dipole moment and radiative recombination lifetime of excitons in WSe2, Jin et. al., Advanced Functional Material,2017.

[10] Mesoscopic electron transport,Lydia L. et. al.,Series E: Applied Sciences, Volume 345.

[11]SPIN-PHOTON ENTANGLEMENT AND QUANTUM OPTICS WITH SINGLE QUANTUM DOTS, John Schaibley Ph.D. Thesis, 2013.

[12] Top-Down Etched Site-Controlled InGaN/GaN Quantum Dots, Lei Zhang, Ph.D. Thesis, 2015.

[13]https://www.osapublishing.org/view$_article.cfm?gotourl$=https%3A%2F%2Fwww%2Eosapubli
FF88-BDF0-591B8D8DD7CCD014$_8$9829%2$Fol-31-11-1738%2Epdf%3Fda%3D1%26id%3D898
$University%20of%20Michigan$

[14] Single Photon Generation & Application in Quantum Cryptography,https://www.physik.huberlin.de/de/nano/lehre/quantenoptik09/singlephoton.

[15]Solid state single photon emitters, Igor Aharonovich et.al., Nature photonics, 2016.

[16]Bennett, C. and Brassard, G., Quantum cryptography: Public key distribution and coin tossing, International Conference on Computers, Systems & Signal Processing, 1984.

[17] Xiao, M., Wu, L., and Kimble, H., Precision measurement beyond the shot-noise limit, Physical review letters, Vol. 59, No. 3, 1987, pp. 278281.

[18] Polzik, E., Carri, J., and Kimble, H., Spectroscopy with squeezed light, Physical review letters, Vol. 68, No. 20, 1992, pp. 30203023

[19] Rarity, J., Owens, P., and Tapster, P., Quantum Random-number Generation and Key Sharing, Journal of Modern Optics, Vol. 41, No. 12, Dec. 1994, pp. 24352444.

[20] Shih, Y. H. and Alley, C. O., New Type of Einstean-Podolsky-Rosen-Bohm Experiment Using Pairs of Light Quanta Produced by Optical Parametric Down Conversion, Physical Review Letters, Vol. 61, No. 26, 1988, pp. 29212924.

[21]Fattal, D., Inoue, K., Vuckovic, J., Santori, C., Solomon, G., and Yamamoto, Y., Entanglement Formation and Violation of Bells Inequality with a Semiconductor Single Photon Source, Physical Review Letters, Vol. 92, No. 3, Jan. 2004, pp. 037903.

[22]Ghali, M., Ohtani, K., Ohno, Y., and Ohno, H., Generation and control of polar-

izationentangled photons from GaAs island quantum dots by an electric field. Nature communications, Vol. 3, Jan. 2012, pp. 661.

[23]Singh, R. and Bester, G., Nanowire Quantum Dots as an Ideal Source of Entangled Photon Pairs, Physical Review Letters, Vol. 103, No. 6, Aug. 2009, pp. 063601.

[24] Introduction to Solid State Physics, Kittle 8th Edition.

[25] Carrier gas and position effects on GaN growth in a horizontal HVPE reactor: An experimental and numerical study,C.E.C.DamP.R.HagemanP.K.Larsen,Science Direct,2005.

[26] Structural defects in GaN revealed by transmission electron microscopy, Zuzanna Liliental-Weber 2014 Jpn. J. Appl. Phys. 53 100205

[27] Inhibition, Enhancement, and Control of Spontaneous Emission in Photonic Nanowires, Joel Bleuse, Julien Claudon, Megan Creasey, Nitin. S. Malik, and Jean-Michel Gerard,PHYSICAL REVIEW LETTERS,2011.

[28]*I. Friedler, C. Sauvan, J. P. Hugonin, P. Lalanne, J. Claudon, and J. M. Gérard, "Solid-state single photon sources: the nanowire antenna," Opt. Express 17,* 2095-2*11*0 *(*2009*)*

[29] Two-Dimensional Transition-Metal Dichalcogenides,Kolobov, Alexander V., Tominaga, Junji, 2016.

[30]Photoluminescence from Chemically Exfoliated MoS2,Goki Eda, Hisato Yamaguchi, Damien Voiry, Takeshi Fujita, Mingwei Chen, and Manish Chhowalla, Nano letters, 2011.

[31] Thermally Driven Crossover from Indirect toward Direct Bandgap in 2D Semiconductors: MoSe2 versus MoS2, Sefaattin Tongay, Jian Zhou, Can Ataca, Kelvin Lo, Tyler S. Matthews, Jingbo Li, Jeffrey C. Grossman, and Junqiao Wu.

[32] Valley-selective circular dichroism of monolayer molybdenum disulphide,Ting

Cao, Gang Wang, Wenpeng Han, Huiqi Ye, Chuanrui Zhu, Junren Shi, Qian Niu, Pingheng Tan, Enge Wang, Baoli Liu & Ji Feng,2012.

[33] kp theory for two-dimensional transition metal dichalcogenide semiconductors, Andor Kormanyos et. al.,arxiv,1410.6666, 2015.

[34] Optical generation of excitonic valley coherence in monolayer WSe2,Aaron M. Jones,Hongyi Yu, Nirmal J. Ghimire,Sanfeng Wu,Grant Aivazian,Jason S. Ross5,Bo Zhao1 , Jiaqiang Yan, David G. Mandrus, Di Xiao, Wang Yao and Xiaodong Xu

[35] Valley-dependent optoelectronics from inversion symmetry breaking,Wang Yao, Di Xiao, and Qian Niu,APS, 2008.

[36] Optical generation of excitonic valley coherence in monolayer WSe2,Aaron M. Jones,Hongyi Yu, Nirmal J. Ghimire,Sanfeng Wu,Grant Aivazian,Jason S. Ross5,Bo Zhao1 , Jiaqiang Yan, David G. Mandrus, Di Xiao, Wang Yao and Xiaodong Xu

[37] The quantum theory of light,Louden, Oxford, 1983.

[38] Cohen-Tannoudji, Atom Photon Ineractions, Wiley-Interscience Publication,1992.

[39] Berman& Malinovsky, Principle of Spectroscopy and Quantum Optics, Princeton University press

[40]Con-focal Optical Microscopy: Robert H Webb IOP Publishing Ltd. 1995

[41]Confocal scanning optical microscope using single-mode fiber for signal detection: Shigeharu Kimura and Tony Wilson: Applied Optics, 1 June 1991/Vol. 30 No. 16

[42] Excitation and scattering of modes on a dielectric or optical fiber, IEEE A.W. Synder 1969

[43]Chromatic polarization of light,German, unknown, 1895

[44]Studies on depolarization of light at microscope lens surfaces- Shinya Inoue PhD presentation

[45]Polarization aberration caused by differential transmission and phase shift in

high-NA lenses: theory, measurement, and rectification: Shribak et. Al Optical engineering 41 (5) 943 954 (May 2002).

[46] Diffraction image in polarization microscope: Hiroshi Kubota and Shinya Inoue: Journal of the Optical Society of America.

[47]Measuring protein concentration with entangled photons Andrea Crespi, Mirko Lobino, Jonathan C. F. Matthews, Alberto Politi, Chris R. Neal, Roberta Ramponi, Roberto Osellame, and Jeremy L. OBrien, Appl. Phys. Lett. 100, 233704 (2012);